



High pressure thermoelasticity and sound velocities of Fe-Ni-Si alloys

Rachel A. Morrison^{a,b,*}, Jennifer M. Jackson^{a,**}, Wolfgang Sturhahn^a, Jiyong Zhao^c, Thomas S. Toellner^c

^a Seismological Laboratory, California Institute of Technology, Pasadena, CA, USA

^b ExxonMobil Upstream Integrated Solutions, Spring, TX, USA

^c Advanced Photon Source, Argonne National Laboratory, Argonne, IL, USA



ARTICLE INFO

Keywords:

Earth's core
Sound velocity
Grüneisen parameter
High pressure
Nuclear resonant inelastic X-ray spectroscopy

ABSTRACT

The Earth's iron-dominant core is known to contain nickel from cosmochemical analysis and some amount of light elements from geophysical constraints on density and seismic wave velocities. Although there have been several studies to constrain thermoelastic properties of iron-alloys, there has been no systematic study on the effects of nickel and light elements on properties of iron using the same experimental methods and data analysis approach. We conducted nuclear resonant inelastic X-ray scattering and X-ray diffraction experiments on body-centered cubic and hexagonal close-packed (hcp) $\text{Fe}_{0.91}\text{Ni}_{0.09}$ and $\text{Fe}_{0.8}\text{Ni}_{0.1}\text{Si}_{0.1}$ up to 104 GPa and 86 GPa, respectively, and compare to similar measurements conducted on hcp-Fe up to 171 GPa. Specifically, we determine the Debye sound velocity from the low-energy transfer region of the (partial) phonon density of states (DOS) using the equation of state determined for each material and a new approach which utilizes information criteria and probability distributions. Nickel decreases the shear velocity of iron, while 10 at% Si has little to no effect on the shear velocity of $\text{Fe}_{0.91}\text{Ni}_{0.09}$. We observe that the shape of the phonon DOS of these alloys remains similar with increasing pressure. In the measured compression range, we therefore apply a generalized scaling law to describe the volume dependence of the phonon DOS and find that the vibrational Grüneisen parameters of hcp- $\text{Fe}_{0.91}\text{Ni}_{0.09}$ are nearly indistinguishable from those hcp-Fe and those for $\text{Fe}_{0.8}\text{Ni}_{0.1}\text{Si}_{0.1}$ trend lower. From the vibrational free energy, we constrain the harmonic vibrational component of thermal pressure, which shows a significant positive deviation from theoretical calculations of hcp-Fe at pressures and temperatures of Earth's core. Collectively, our results demonstrate that the effects of nickel should be considered when modeling iron-rich planetary cores.

1. Introduction

Seismological observations place constraints on the shear and compressional sound velocities and density of the inner core (e.g., Dziewonski and Anderson, 1981; Kennett et al., 1995) and the discontinuity in compressional sound velocity and density at the inner core boundary (e.g., Deuss, 2008; Masters and Gubbins, 2003). These observations, in conjunction with cosmochemical and mineral physics studies, place constraints on the composition and thermal profile of the inner core. The density of the inner core is ~3–5% lighter than hcp-iron at inner core conditions (reviewed in Li and Fei 2014), which supports the presence of light elements in the inner core. Thus many studies have focused on quantifying the effects of alloying iron with lighter elements on the density of pure iron, lending support to the presence of light elements such as Si, O, S, C, H in the inner core (reviewed in Hirose et al.,

2013; Li and Fei, 2014; Litasov and Shatskiy, 2016; Vočadlo, 2015). A plausible inner core composition must also match the compressional and shear velocities of the inner core, which are reported to be respectively ~4–10% slower (e.g., Sakamaki et al., 2016) and >30% slower than hcp-iron (e.g., Martorell et al., 2013a).

A detailed understanding of the effect of composition on the sound velocities and densities of iron alloys at core pressures and temperatures is necessary to constrain the inner core composition and the melting temperature at the inner core boundary, as well as to better constrain outer core composition and to understand the nature of anisotropy and heterogeneity in the inner and outer core. Furthermore, an understanding of the thermoelastic properties of these alloys at core conditions can help constrain geodynamical simulations of the evolution and ongoing processes of the core.

The sound velocities of hcp-iron have been extensively studied

* Correspondence to: R.A. Morrison, ExxonMobil Upstream Integrated Solutions, Spring, TX, USA.

** Corresponding author.

E-mail addresses: rachel.a.morrison@exxonmobil.com (R.A. Morrison), jackson@gps.caltech.edu (J.M. Jackson).

through shockwave experiments (Brown and McQueen, 1986; Jeanloz, 1979; Nguyen and Holmes, 2004), 300 K static compression experiments (Antonangeli et al., 2004, 2018; Decremps et al., 2014; Giefers et al., 2002; Gleason et al., 2013; Lin et al., 2005; Liu et al., 2014, 2016; Lübbbers et al., 2000; Mao et al., 2001, 2008, 2012; Murphy et al., 2013; Ohtani et al., 2013), high temperature static compression experiments (Lin et al., 2005; Mori et al., 2017; Sakamaki et al., 2016), and ab initio studies (Laio et al., 2000; Mao et al., 2001; Martorell et al., 2013a; Niu et al., 2015; Steinle-Neumann et al., 2001; Vočadlo et al., 2009). Similarly, numerous experimental and ab initio studies have investigated hcp-iron's isothermal equation of state (e.g., Boehler et al., 2008; Dewaele et al., 2006; Dubrovinsky et al., 2000; Mao et al., 1990; Ono et al., 2010; Steinle-Neumann et al., 1999) and thermal equation of state (Dubrovinsky et al., 1998; Fei et al., 2016; Garai et al., 2011; Sakai et al., 2014; Sha and Cohen, 2010; Stixrude et al., 1997; Uchida et al., 2001; Wasserman et al., 1996; Yamazaki et al., 2012).

An important element in constraining the thermal equation of state of hcp-iron is the thermal Grüneisen parameter, which relates thermal pressure to thermal energy per unit volume and can be used to reduce shock data for comparison with isothermal compression studies. As the thermal Grüneisen parameter is composed of vibrational and electronic contributions, constraints on hcp-iron's vibrational Grüneisen parameter have helped further constrain its thermal equation of state (Dewaele et al., 2006; Dubrovinsky et al., 2000; Murphy et al., 2011a; Uchida et al., 2001; Yamazaki et al., 2012). Furthermore, hcp-iron's thermal pressure can be estimated by pairing the vibrational component of thermal pressure, directly accessed through phonon density of states (DOS) measurements (Murphy et al., 2011b), with ab initio constraints on the electronic and anharmonic components of thermal pressure (Alfè et al., 2001; Dewaele et al., 2006; Martorell et al., 2013a, 2013b; Sha and Cohen, 2010; Wasserman et al., 1996).

Despite the presence of nickel in the Earth's core (Allègre et al., 1995; McDonough and Sun, 1995; McDonough, 2003), the sound velocities and thermoelasticity of hcp-structured iron-nickel alloys have received comparatively little attention. Lin et al., (2003) determined the shear and compressional sound velocities of bcc- and hcp- $\text{Fe}_{0.92}\text{Ni}_{0.08}$ with nuclear resonant inelastic X-ray scattering (NRIXS) and found nickel slightly decreased the compressional and shear velocities of hcp-Fe for a given density. However, there was considerable scatter in the data of iron (Mao et al., 2001) and iron-nickel, such that no effect could also be concluded from these measurements. A variety of experimental studies investigated the equations of state of hcp-iron-nickel at 300 K (Mao et al., 1990; Morrison et al., 2018; Takahashi et al., 1968) as well as at high temperatures (Asanuma et al., 2011; McQueen and Marsh, 1966; Sakai et al., 2014). However, constraints on the thermal equations of state of hcp-iron-nickel are limited and indicate a considerable range of thermal parameters associated with the effects of nickel (Côté et al., 2012; Ekholm et al., 2011; Martorell et al., 2013a).

Silicon is a favored light element in the inner core for a variety of reasons, including its abundance in the Earth's mantle, the magnesium to silicon ratio in the crust and mantle of Earth compared to chondritic meteorites (Allègre et al., 2001, 1995), observations that silicon partitions into iron in silicate-iron partitioning experiments conducted at high pressure and high temperature (Fischer and Campbell, 2015; Ricolleau et al., 2011), and ab initio and experimental results demonstrating silicon partitions roughly equally between liquid and solid iron at high pressure (Alfè et al., 2002, 2007).

A variety of studies have investigated the sound velocities of iron-silicon alloys at 300 K (Antonangeli et al., 2018; Badro et al., 2007; Lin et al., 2003; Liu et al., 2014; Mao et al., 2012; Ono, 2013; Sakairi et al., 2018). Silicon is found to increase the compressional velocity of hcp-Fe, but the effect of silicon on hcp-Fe's shear velocity is debated. Recently, Sakairi et al. (2018) investigated the compressional wave velocity of hcp- $\text{Fe}_{0.89}\text{Si}_{0.11}$ up to 1800 K and 84 GPa with inelastic X-ray scattering (IXS), better constraining effect of silicon on compressional

velocity at higher temperatures. Fewer studies have investigated the sound velocities of iron-nickel-silicon alloys at 300 K: Antonangeli et al. (2010) determined the compressional wave velocity from phonon dispersion measurements and Liu et al. (2016) constrained the shear wave velocities from NRIXS measurements. Most constraints on iron-silicon sound velocities at inner core conditions come from ab initio studies (Vočadlo, 2007; Tsuchiya and Fujibuchi, 2009; Ono, 2013; Martorell et al., 2016). Isothermal equations of state of these alloys include Lin (2003), Hirao et al. (2004), Ono et al. (2007), Sata et al. (2010), Asanuma et al. (2011), Tateno et al. (2015), Morrison et al. (2018), and experimental thermal equations of state studies include Zhang and Guyot (1999), Fischer et al. (2012, 2014), Tateno et al. (2015), all utilizing X-ray diffraction techniques. However, to date, the thermal properties of iron-nickel-silicon alloys, including constraints on the Grüneisen parameter, have not been investigated with techniques sensitive to the vibrational properties of the material.

We present NRIXS measurements on bcc- and hcp- $\text{Fe}_{0.91}\text{Ni}_{0.09}$ and $\text{Fe}_{0.8}\text{Ni}_{0.1}\text{Si}_{0.1}$ up to 104 GPa and 86 GPa, respectively. To ensure a systematic comparison with hcp-Fe by avoiding differences in analyses methods, we re-analyze hcp-Fe NRIXS data from Murphy et al. (2011a, 2011b, 2013). We present derived partial (projected) phonon density of states for each composition. We determine the Debye sound velocity from the low energy region of the phonon density of states using a new analysis method utilizing probability density functions which better constrains the Debye sound velocity and its uncertainty from the measured data. We present two separate constraints on the vibrational component of thermal pressure for the hcp phases. First, we determine the Grüneisen parameter by applying a volume scaling relation to the phonon DOSs. Second, we estimate vibrational thermal pressure from the vibrational free energy derived from the phonon DOS. The thermal expansion is determined using constraints on the bulk modulus from the same alloys (Morrison et al., 2018). Additional parameters are derived from the phonon DOS including the vibrational kinetic energy, vibrational heat capacity, and Lamb-Mössbauer factor.

2. Experimental methods

Samples were synthesized by arc-melting individual pieces of Ni, Si, and 95%-enriched ^{57}Fe in an argon atmosphere to produce $\text{Fe}_{0.91}\text{Ni}_{0.09}$ and $\text{Fe}_{0.8}\text{Ni}_{0.1}\text{Si}_{0.1}$. Samples were then cold rolled to $\sim 10 \mu\text{m}$. SEM measurements confirmed the molar sample compositions to be $\text{Fe}_{0.91(1)}\text{Ni}_{0.09(1)}$ and $\text{Fe}_{0.80(1)}\text{Ni}_{0.10(1)}\text{Si}_{0.10(1)}$, and sample homogeneity was observed at a scale of $1 \mu\text{m}$. Samples from this synthesis batch were previously used to constrain the melting temperature of $\text{Fe}_{0.91}\text{Ni}_{0.09}$ (Zhang et al., 2016) and to constrain the equations of state of $\text{Fe}_{0.91}\text{Ni}_{0.09}$ and $\text{Fe}_{0.8}\text{Ni}_{0.1}\text{Si}_{0.1}$ (Morrison et al. (2018)).

High pressure conditions were achieved using modified panoramic diamond anvil cells (DACs) with 90° openings and cubic boron nitride backing seats on the downstream side. These modifications maximize the accessible angle range for in situ X-ray diffraction (XRD). One $\text{Fe}_{0.91}\text{Ni}_{0.09}$ and one $\text{Fe}_{0.8}\text{Ni}_{0.1}\text{Si}_{0.1}$ experimental run (hereafter referred to as FeNi-Run#1 and FeNiSi-Run#1) were each conducted with beryllium gaskets and loaded with a neon pressure medium at Caltech to ensure nearly hydrostatic conditions. These experimental runs focused on lower pressures where both $\text{Fe}_{0.91}\text{Ni}_{0.09}$ and $\text{Fe}_{0.8}\text{Ni}_{0.1}\text{Si}_{0.1}$ were in the bcc phase. An $\text{Fe}_{0.91}\text{Ni}_{0.09}$ and an $\text{Fe}_{0.8}\text{Ni}_{0.1}\text{Si}_{0.1}$ experimental run (FeNi-Run#2 and FeNiSi-Run#2) were each prepared with a beryllium gasket and a boron-epoxy insert to stabilize the chamber at higher pressures, and then loaded with a neon pressure medium. An $\text{Fe}_{0.8}\text{Ni}_{0.1}\text{Si}_{0.1}$ experimental run (FeNiSi-Run#3) was prepared with a beryllium gasket and a boron-epoxy insert with no additional pressure medium. Additional bcc- $\text{Fe}_{0.91}\text{Ni}_{0.09}$ and $\text{Fe}_{0.8}\text{Ni}_{0.1}\text{Si}_{0.1}$ foil samples were placed on Kapton tape for ambient pressure measurements. Powdered 95%-enriched ^{57}Fe was also placed on Kapton tape for an ambient pressure measurement of bcc-Fe.

We collected nuclear resonant scattering measurements on each

sample at 300 K at Sector 3-ID-B at the Advanced Photon Source. The storage ring was run with 24-bunch top-up mode, with each bunch separated by 153 ns. Incoherent inelastic X-ray scattering was measured with three avalanche photodiode detectors (APDs) positioned radially around the sample, and forward elastic scattering was measured with a single APD downstream from the sample to constrain the resolution function. The X-ray energy was tuned around the nuclear resonance of ^{57}Fe (14.4125 keV) with a high-resolution monochromator (Toellner, 2000). We varied the scanned energy range depending on the sample and the pressure (a summary is provided in Table S1). For $\text{Fe}_{0.91}\text{Ni}_{0.09}$ measurements, higher counting rates at lower pressures motivated moderately larger scanned energy ranges for the bcc compression points. Compared with $\text{Fe}_{0.91}\text{Ni}_{0.09}$, we observed higher energy phonon modes for $\text{Fe}_{0.8}\text{Ni}_{0.1}\text{Si}_{0.1}$, which motivated the use of larger scanned energy ranges for some compression points. The higher energy modes observed in $\text{Fe}_{0.8}\text{Ni}_{0.1}\text{Si}_{0.1}$ are likely due to more dispersive optical phonon branches in the Fe-Ni-Si alloy compared with those in $\text{Fe}_{0.91}\text{Ni}_{0.09}$ and Fe (e.g., Muñoz, 2013; Wakabayashi et al., 1982). The typical energy resolution (full width at half maximum at zero energy transfer) was 1.1 meV. There were four $\text{Fe}_{0.91}\text{Ni}_{0.09}$ compression points between 83 and 104 GPa where we observed large tails around the resolution peak, which severely impacted the quality of the data, so these compression points were discarded. The X-rays were focused to an area of 10 by 14 μm^2 using a Kirkpatrick-Baez mirror system. The nuclear resonant inelastic X-ray scattering (NRIXS) spectra for bcc-Fe, $\text{Fe}_{0.91}\text{Ni}_{0.09}$, and $\text{Fe}_{0.8}\text{Ni}_{0.1}\text{Si}_{0.1}$ at 0 GPa are compared in Fig. 1. The

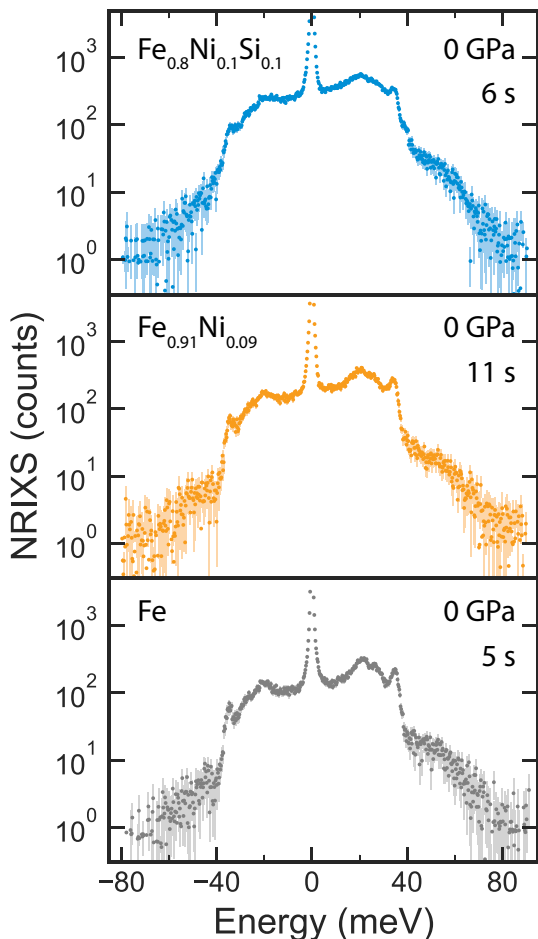


Fig. 1. Comparison of raw (unnormalized) NRIXS spectra for bcc-Fe_{0.91}Ni_{0.09}, Fe_{0.8}Ni_{0.1}Si_{0.1}, and Fe at 0 GPa and 300 K collected around the resonance energy of ^{57}Fe at 14.5125 keV with a step size of 0.25 meV. The numbers in the upper left of each panel indicate the collection time per data point.

NRIXS spectra for all compression points are plotted in Figs. S1 and S2 in the Supplementary material.

In situ X-ray diffraction (XRD) was collected before and after each set of NRIXS scans and averaged to determine the unit-cell volume of the sample at each pressure point (e.g., Gao et al., 2009; Murphy et al., 2013). The X-ray wavelength energy was 14.4125 keV (0.086 nm), corresponding to a nuclear resonance of ^{57}Fe . The XRD images were calibrated with a powdered CeO₂ sample and integrated with the Dioptas software package (Prescher and Prakapenka, 2015). We fit the resulting X-ray diffraction patterns with full-profile Pawley refinement to determine the bcc phase lattice parameter a using reflection (100) and the hcp phase lattice parameters a and c using reflections (100), (101), and (002). We observed the decay/loss of intensity in the (002) reflection in several of the compression points of hcp-Fe_{0.91}Ni_{0.09} and hcp-Fe_{0.8}Ni_{0.1}Si_{0.1} and interpret this as texture development. The remaining diffraction reflections for these compression points were sufficient to determine a and c , as the (100) reflection is sensitive to the a lattice parameter and the (101) reflection is sensitive to both the a and c lattice parameters. A preliminary estimate of the lattice parameter uncertainty comes from results of the Pawley refinements. XRD measurements conducted at APS GSECARS sector 13-BM-C ($E = 28.57$ keV) on the same DAC at select compression points showed that the deviations resulting from use of about four times the amount of reflections are within a doubling of the uncertainties provided from the Pawley refinements. We therefore double the uncertainties provided by the Pawley refinements for all Fe_{0.91}Ni_{0.09} and Fe_{0.8}Ni_{0.1}Si_{0.1} compression points. The resulting lattice parameters and unit-cell volumes are reported in Table 1.

Density was determined from the in situ unit-cell volume measurements and accounts for the 95% ^{57}Fe isotopic enrichment of the samples (Table 1). Throughout most of the NRIXS data analysis, we relied on the measured in situ volumes and densities. We convert the unit-cell volumes to pressure using the equations of state (EOSs) for each sample. For the bcc-Fe data, we use the Vinet EOS reported in Morrison et al. (2018) based on compression data from Dewaele et al. (2006). For bcc- and hcp-Fe_{0.91}Ni_{0.09} and Fe_{0.8}Ni_{0.1}Si_{0.1}, we use the Vinet EOSs also reported in Morrison et al. (2018). These EOSs were determined from samples synthesized from the same Fe_{0.91}Ni_{0.09} and Fe_{0.8}Ni_{0.1}Si_{0.1} batches used in the NRIXS experiments. All of the EOSs referenced in this study were determined using the same pressure transmitting medium (helium) and the same pressure calibrant (tungsten with the Dorogokupets and Oganov (2006) pressure scale). The experimental conditions and resulting parameters from each EOS study are listed in Table S2. The resulting pressure, K_T , and K_T' are listed in Table 1. The conversion to adiabatic bulk moduli utilizes thermodynamic parameters constrained in this study and will be discussed later.

The NRIXS data were analyzed with the PHOENIX software package (version 3.0, www.NRIXS.com) to obtain the partial phonon density of states (DOS) $D(E, V_i)$, Debye sound velocity, and other vibrational-related quantities, including the Lamb-Mössbauer factor, kinetic energy, thermal expansion, and free energy. As detailed in Sturhahn (2000, 2004) and Sturhahn and Jackson (2007), the background and the measured elastic peak were fitted and subtracted from the measured NRIXS spectrum to obtain the pure phonon excitation spectrum, $I'(E)$. The excitation probability density $S(E, V_i)$ was then obtained by applying a normalization procedure to $I'(E)$ based on the property that the first moment of $S(E, V_i)$ is equal to the recoil energy of the resonant isotope E_R . For ^{57}Fe , $E_R = 1.956$ meV. PHOENIX applies the Fourier-log method to decompose $S(E, V_i)$ into n -phonon contributions,

$$S_n(E, V_i) = \int E^n S(E, V_i) dE, \quad (1)$$

for $n = 0, 1, 2, 3$. For example, the Lamb-Mössbauer factor and the kinetic energy can be directly determined from the 0th- and 2nd-order moments $S_0(E, V_i)$ and $S_2(E, V_i)$, respectively (see Sections 3 and 5 in the

Table 1

Results from X-ray diffraction and 300 K equations of state.

Phase	<i>a</i>	<i>c</i>	Volume	Density ^a	Pressure ^b	<i>K_T</i>	<i>K_{T'}</i>
	(Å)	(Å)	(Å ³)	(g/cm ³)	(GPa)	(GPa)	
bcc-Fe	2.863(1)		23.46(3)	8.062(9)	0	168(8)	4.7(1.3)
	2.874(1)		23.73(2)	7.99(1)	0	147(3)	6.4(6)
	2.859(1)		23.38(3)	8.11(1)	1.7(1)	158(2)	6.3(6)
	2.847(1)		23.08(3)	8.22(1)	3.8(1)	171(1)	6.1(6)
	2.843(1)		22.98(3)	8.25(1)	4.5(1)	175(1)	6.1(5)
	2.825(1)		22.54(2)	8.41(1)	8.1(1)	196(2)	5.9(5)
	2.454(1)	3.948(2)	20.59(2)	9.21(1)	18.0(1)	251(2)	4.88(7)
	2.438(1)	3.925(4)	20.21(3)	9.38(1)	22.8(2)	274(2)	4.77(7)
	2.399(2)	3.831(10)	19.09(6)	9.93(3)	41(1)	357(1)	4.46(6)
	2.389(1)	3.788(7)	18.72(4)	10.13(2)	48(1)	388(1)	4.37(6)
hcp-Fe _{0.91} Ni _{0.09}	2.359(1)	3.748(6)	18.07(4)	10.50(2)	63(1)	453(1)	4.22(6)
	2.341(1)	3.708(4)	17.60(2)	10.77(1)	75(1)	504(2)	4.12(5)
	2.330(1)	3.687(5)	17.33(3)	10.94(2)	83(1)	538(2)	4.06(5)
	2.299(1)	3.654(9)	16.72(4)	11.34(3)	104(3)	620(3)	3.94(5)
	2.859(1)		23.38(3)	7.70(1)	0	156(8)	5.7(1.2)
	2.821(1)		22.46(2)	8.02(1)	7.1(1)	194(2)	5.3(1.1)
	2.824(1)		22.53(3)	8.00(1)	6.5(1)	191(2)	5.3(1.1)
	2.432(1)	3.886(6)	19.9(3)	9.05(2)	27.9(3)	281(2)	5.12(6)
	2.408(1)	3.846(8)	19.31(5)	9.33(2)	37.1(6)	327(2)	4.94(6)
	2.379(2)	3.896(10)	19.09(6)	9.44(3)	41(1)	347(2)	4.88(6)
bcc-Fe _{0.8} Ni _{0.1} Si _{0.1}	2.366(1)	3.796(9)	18.40(5)	9.79(3)	55(1)	413(1)	4.70(6)
	2.346(1)	3.740(7)	17.83(4)	10.10(2)	69(1)	478(1)	4.56(6)
	2.331(2)	3.669(10)	17.26(6)	10.44(4)	86(3)	553(2)	4.43(5)

^a Density calculations account for sample enrichment.^b Pressure, isothermal bulk modulus (*K_T*), and pressure derivative of bulk modulus (*K_{T'}*) were calculated from volumes paired with Vinet EOSs listed in Table S2 in the Supplementary material (Morrison et al., 2018).

Supplementary material).

To obtain the phonon DOS from $S_1(E, V_i)$, the quasi-harmonic approximation was applied, which assumes the interatomic potential is harmonic and accounts for thermal expansion. This approximation is thought to be reasonable for measurements of iron-rich alloys at 300 K (Alfé et al., 2001). The resulting projected partial phonon DOS $D(E, V_i)$ was normalized by $\int D(E, V_i)dE = 3$. The phonon DOS is ‘projected’ due to the dependency on the direction of incident X-rays and ‘partial’ as NRIXS is sensitive to the resonant isotope ^{57}Fe . Thus for the ^{57}Fe samples in this study, the results are simply the projected phonon DOS. For the bcc phase, $D(E, V_i)$ is isotropic (Sturhahn and Kohn, 1999). For samples in the hcp phase, the dependency on the angle of incident X-rays should be minimal as the samples are polycrystalline and, in most cases, loaded with neon as a pressure medium. Additionally, anisotropy of the phonon DOS for hcp-Fe was found to be minimal in the low energy region used for sound velocity determinations (Giefers et al., 2002), and anisotropy in the compressional elastic components for these iron-alloys was also found to be minimal at 300 K (Morrison et al., 2018). Because the alloys studied here are predominantly iron (using 95%-enriched ^{57}Fe), the partial phonon DOS is a very close approximation to the total phonon DOS. The resulting phonon DOSs for bcc and hcp phases are plotted in Figs. 2 and 3, respectively.

To compare our results to those of hcp-iron in a consistent manner, we re-analyzed data from the NRIXS study on hcp-iron by Murphy et al. (2011a, 2011b, 2013) using the same methods as for Fe_{0.91}Ni_{0.09} and Fe_{0.8}Ni_{0.1}Si_{0.1} described throughout this paper. The resulting phonon DOSs for hcp-iron are plotted in Fig. 3. We excluded the 36 GPa hcp-Fe NRIXS dataset from our re-analysis, as we found the statistical quality to be inferior to the other scans in this study. The 36 GPa dataset was collected over a much shorter integration time (18 s, compared to an average of 53 s), and the number of counts for the highest intensity peak in the Stokes region was much smaller (70 counts, compared to an average of 183 counts).

We compare the phonon DOS of the bcc and hcp phases of Fe, Fe_{0.91}Ni_{0.09}, and Fe_{0.8}Ni_{0.1}Si_{0.1} in Fig. 4. The phonon DOSs for the bcc phases are plotted as measured at 0 GPa. The total phonon DOS for hcp-

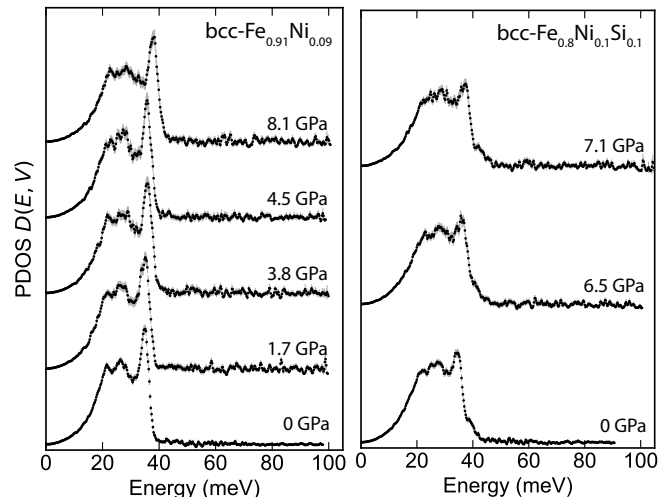


Fig. 2. Partial phonon density of states (DOS) of bcc-Fe_{0.91}Ni_{0.09} and Fe_{0.8}Ni_{0.1}Si_{0.1}. Phonon DOSs are offset for visibility. Pressures were determined from unit-cell volumes measured in situ.

Fe at 90 GPa, and the partial phonon DOSs for hcp-Fe_{0.91}Ni_{0.09} at 48 GPa and for hcp-Fe_{0.8}Ni_{0.1}Si_{0.1} at 41 GPa are scaled to 0 GPa using the phonon DOS scaling method outlined in Section 4. Note the difference in relative phonon mode intensity between bcc- and hcp-structured iron alloys. Also, note the differences between the phonon DOSs of different compositions. For instance, the phonon DOSs of bcc- and hcp-Fe_{0.8}Ni_{0.1}Si_{0.1} extend to higher energies than the phonon DOSs of Fe and Fe_{0.91}Ni_{0.09}.

3. Sound velocities

3.1. Debye sound velocity

The Debye sound velocity (v_D) can be determined from the low-

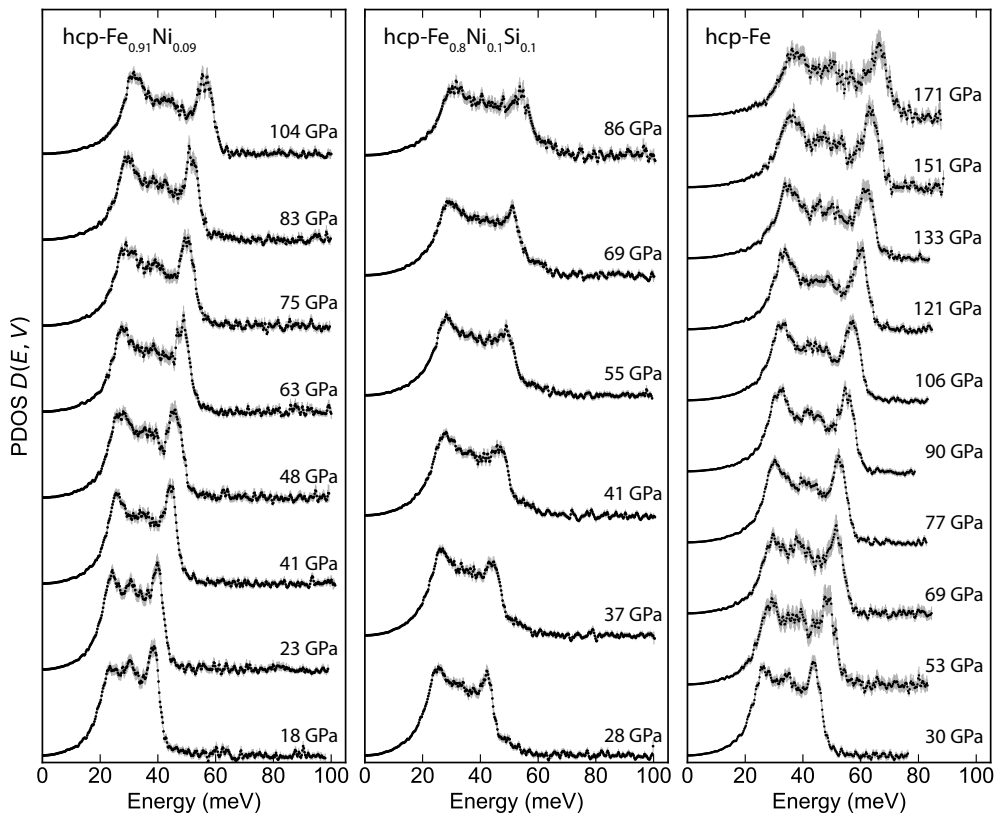


Fig. 3. Partial phonon density of states (DOS) of hcp-Fe_{0.91}Ni_{0.09} and Fe_{0.8}Ni_{0.1}Si_{0.1} and total phonon DOS of hcp-Fe re-analyzed from Murphy et al. (2013). Spectra are offset for visibility. Pressures were determined from unit-cell volumes measured in situ.

energy region of the phonon DOS via

$$\nu(E) = \left[\frac{\tilde{m}}{2\pi^2 \hbar^3 \rho} \frac{1}{D(E)} E^2 \right]^{1/3}, \quad (2)$$

where \tilde{m} is the mass of the resonant isotope, ρ is the density of the material being measured, and $\nu(E) = \nu_D$ in the limit where E approaches zero (e.g., Sturhahn, 2004). As an example, we illustrate select phonon DOSs of hcp-Fe, Fe_{0.91}Ni_{0.09}, and Fe_{0.8}Ni_{0.1}Si_{0.1} scaled according to Eq. (2) in Fig. 5. Two different phonon dispersion models are plotted together with the scaled phonon DOSs. A ‘Debye-like’ model varies quadratically (parabolic) with energy and therefore plots as a constant value in Fig. 5. The parabolic ‘Debye-like’ regions of the phonon DOSs of Fe and Fe_{0.91}Ni_{0.09} extend to about 15 meV at these pressures, thus a large enough energy range to obtain a suitable constraint on the Debye velocity using this particular model, whereas assuming the parabolic trend above about 15 meV at this pressure would not be appropriate. The parabolic region of Fe_{0.8}Ni_{0.1}Si_{0.1} at 41 GPa is noticeably smaller than that of Fe_{0.91}Ni_{0.09} at the same pressure. A greater amount of data can be included if instead an empirical power law model of the phonon dispersion curve is applied,

$$\nu(E) = \nu_D [1 - (E/A_1)^4], \quad (3)$$

where the power of 4 is fixed in all cases presented here, and the parameters ν_D and A_1 are fit. In both models of phonon dispersion, the limit of $\nu(E)$ as E approaches zero provides ν_D . For consistency, we apply the phonon dispersion curve in Eq. (3) to the phonon DOSs of both hcp-Fe_{0.91}Ni_{0.09} and Fe_{0.8}Ni_{0.1}Si_{0.1}, as well as to our re-analysis of hcp-Fe data from Murphy et al. (2013) using a new approach presented here. Note that Eq. (3) is a Debye-like model for very large values of A_1 .

The goal is to accurately determine the Debye velocity with an appropriate uncertainty from a measured phonon DOS. An ideal method should be repeatable, consistent, and produce meaningful

uncertainties. Previous selection criteria have involved selecting an energy range that corresponds to a low reduced goodness of fit (χ^2) and a stable ν_D (e.g., Murphy et al., 2013). The metric χ^2 is meaningful in that it detects deviations in the model from the data (i.e., it is sensitive to under-fitting of the data). However, χ^2 is not sensitive to over-fitting of the data, as only a few data points may yield a very good (low) χ^2 . A better choice would be a metric that prefers both a good fit of the model to the data and an energy range with more data points (i.e., a criterion that disfavors both under-fitting and over-fitting of the data). Essentially, an energy range choice should yield the maximum information from the data.

There are a variety of methods of estimating information, some more computationally intensive than others. Two common information estimates that are easily computationally accessible are the Akaike Information Criterion (AIC) and the Bayesian Information Criterion (BIC). Both of these criteria assume a large number of data points. When selecting between energy fit ranges, the number and quality of data points will vary, so it is important to not assume the number of data points is large. A common correction to the AIC (known as the AICc) corrects for the case where the number of data points is small (Hurvich and Tsai, 1989). The AICc has the form

$$AICc = \chi^2 + 2M + \frac{2M(M+1)}{N-M-1}, \quad (4)$$

where χ^2 is the goodness of fit of the model to the data, M is the number of model parameters, and N is the number of data points. In our case, $M = 2$ for a power law model (Eq. (3)) where the model parameters are ν_D and A_1 , and N is the number of data points in the selected energy range. The third term of Eq. (4) is critical, as it provides a sensitivity to over-fitting of the data, which a traditional goodness of fit lacks.

As an example, we plot the effective probability $\exp(-AICc/2)$ of each fit as a function of the start and end of the fit range (E_{min} and E_{max} , respectively) for Fe_{0.91}Ni_{0.09} at 41 GPa in the top panel of Fig. 6. Low

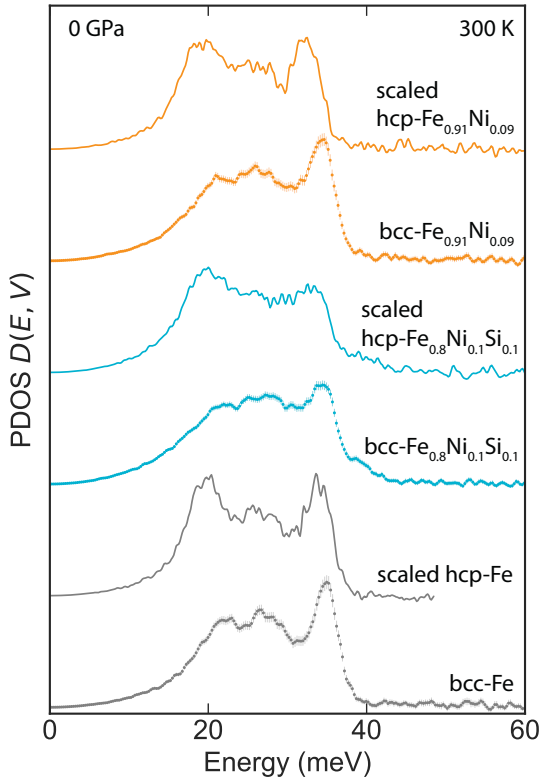


Fig. 4. Partial phonon DOS (PDOS) of bcc-Fe_{0.91}Ni_{0.09}, Fe_{0.8}Ni_{0.1}Si_{0.1} and total PDOS of Fe at 0 GPa are compared to PDOSs scaled to 0 GPa of hcp-Fe_{0.91}Ni_{0.09} (scaled from 48 GPa), Fe_{0.8}Ni_{0.1}Si_{0.1} (scaled from 41 GPa), and Fe (scaled from 90 GPa, re-analyzed from Murphy et al. (2013)). The scaling was accomplished using our determined $\gamma_{0,vib}$ and q for each composition and the scaling procedure detailed in Section 4.

values of $\exp(-AICc/2)$, e.g., where the number of data points is too small or where E_{max} is too large, provide a poor constraint on the Debye velocity v_D , whereas high values of $\exp(-AICc/2)$ provide a better constraint on v_D . This plot demonstrates there are many choices of E_{min} and E_{max} that are equally favorable, e.g., choices that yield equally large values of $\exp(-AICc/2)$. We also plot the v_D as a function of E_{min} and E_{max} in the middle panel of Fig. 6. Depending on the quality of the NRIXS spectrum and the phonon dispersion, the value of v_D obtained from a given data set may vary widely for different fit ranges, even for fit ranges with similar AICc values. As a result, two different fit ranges may yield equal values of $\exp(-AICc/2)$ but noticeably different Debye velocities. By accounting for many possible fit ranges in the calculation of v_D , this method provides a more reasonable constraint on the uncertainty of v_D than would be obtained by using a single energy range. For example, in Fig. 6 we include all fit ranges that fall within $E_{min} = 0.0\text{--}27.0$ meV and $E_{max} = 1.0\text{--}28.0$ meV. This is a demonstration that using this approach leads to a v_D that doesn't depend on the choice of E_{min} . The results we present throughout the manuscript are for $E_{min} = 3.5\text{--}27.0$ meV and $E_{max} = 4.5\text{--}28.0$ meV. The v_D of these fits are weighted by their corresponding $\exp(-AICc/2)$ and binned to produce a probability distribution function of v_D (bottom panel of Fig. 6). The most probable value is then obtained by using two asymmetric functions to fit the probability distribution. The reported Debye velocity and its uncertainty is the peak and FWHM of the best-fit asymmetric function, respectively.

We compare the obtained probability distribution functions for hcp-Fe, Fe_{0.91}Ni_{0.09}, and Fe_{0.8}Ni_{0.1}Si_{0.1} in Fig. 7, each at three different pressures. These probability distribution functions illustrate that the uncertainty on v_D can vary noticeably depending on the quality of the NRIXS data. The increase in v_D with pressure is clearly resolvable given

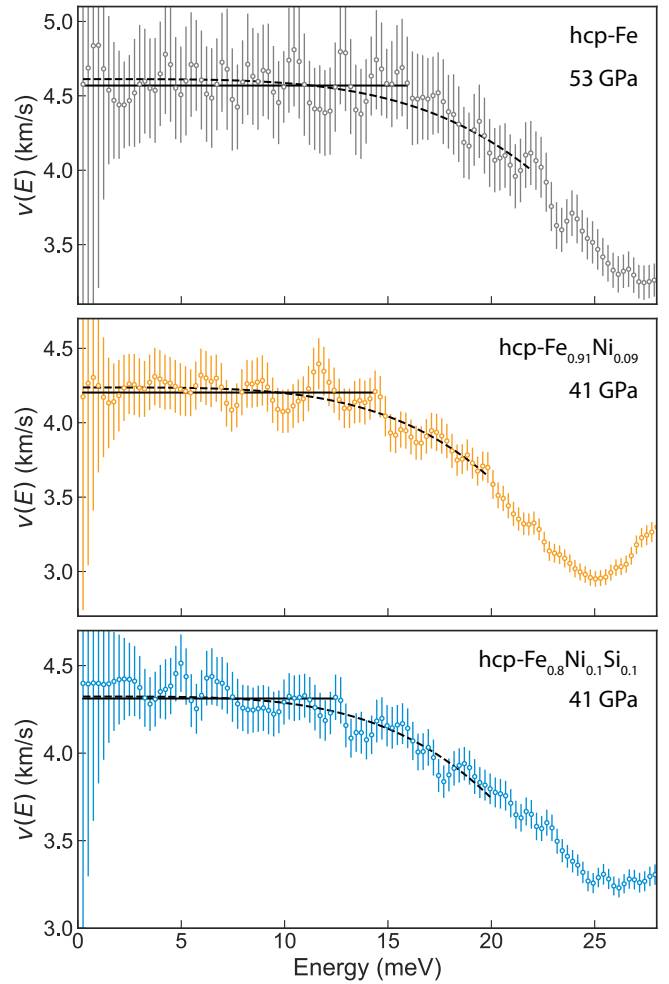


Fig. 5. Phonon DOFs of hcp-Fe, Fe_{0.91}Ni_{0.09}, and Fe_{0.8}Ni_{0.1}Si_{0.1} scaled according to Eq. (2) to allow for visual representation of the low energy region used to constrain the Debye sound velocity. Examples of two typical phonon dispersion models used to constrain the Debye sound velocity are plotted: the Debye-like model (flat black solid line) and the power law model (Eq. (3), black dashed line). The hcp-Fe data is from our re-analysis of Murphy et al. (2013), and all other data is from this study. Fe_{0.91}Ni_{0.09} and Fe_{0.8}Ni_{0.1}Si_{0.1} data were conveniently collected at the same pressure of 41 GPa. The flat region at low energy appropriate for fitting a constant Debye-velocity model is much larger for hcp-Fe_{0.91}Ni_{0.09} than for hcp-Fe_{0.8}Ni_{0.1}Si_{0.1}. We note that the fit models plotted here are purely demonstrative and do not directly reflect our reported Debye velocities. See text for a detailed description of our Debye velocity determination method.

the v_D probability distributions and v_D uncertainty. The Debye velocities for bcc- and hcp-Fe, Fe_{0.91}Ni_{0.09}, and Fe_{0.8}Ni_{0.1}Si_{0.1} computed via this method are listed in Table 2 and plotted as a function of density and pressure in Fig. 8.

We find measurable differences in the Debye velocities of iron and iron-nickel. Alloying hcp-iron with 9 at% nickel decreases the Debye velocity for a given density or pressure. Interestingly, alloying Fe_{0.91}Ni_{0.09} with 10 at% silicon produces Debye velocities very similar to those of pure iron as a function of density, but as a function of pressure, v_D values of Fe_{0.8}Ni_{0.1}Si_{0.1} are similar to those of Fe_{0.91}Ni_{0.09} (Fig. 8). To understand why, we first look to constraints at the lattice level. Morrison et al. (2018), using samples from the same syntheses as those studied here, investigated Fe_{0.91}Ni_{0.09} and Fe_{0.8}Ni_{0.1}Si_{0.1} to ~ 170 GPa in a helium pressure medium using powder X-ray diffraction. Within the experimental resolution, the XRD patterns are consistent with the hcp structure for both compositions. Specifically, there are no additional reflections that would indicate a super-structure

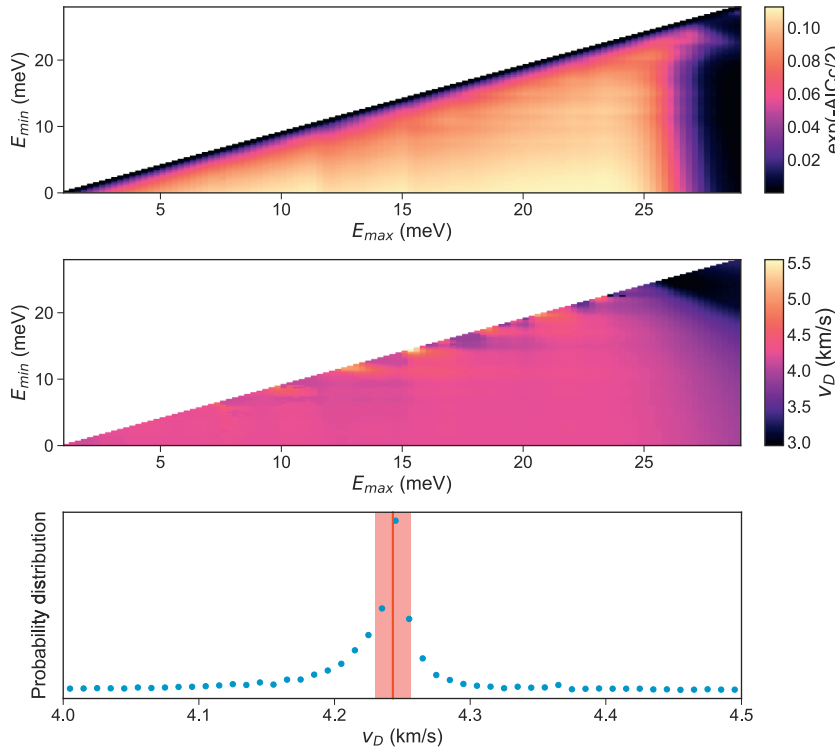


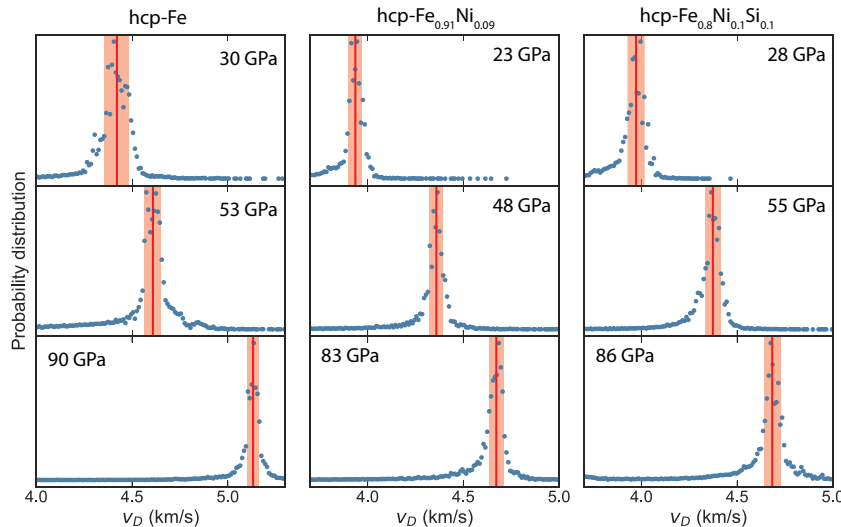
Fig. 6. To illustrate our Debye velocity determination, the power law function (Eq. (3)) is applied to the low energy region of the phonon DOS of hcp- $\text{Fe}_{0.91}\text{Ni}_{0.09}$ at 41 GPa. In the top panel, we plot the fit quality of the model as a function of starting energy range E_{\min} and ending energy range E_{\max} . Fit quality is assessed as $\exp(-\text{AICc}/2)$, where the corrected Akaike Information Criterion (AICc) is defined in Eq. (4). Larger values of $\exp(-\text{AICc}/2)$ represent higher quality fits. In the middle panel, we plot the resulting Debye velocity as a function of E_{\min} and E_{\max} . These variations in Debye velocity highlight the advantage of our Debye velocity analysis method over a fixed energy range, which may influence the resulting Debye velocity. In the bottom panel, we plot the probability distribution of the Debye velocity as calculated from the top two panels using a bin size of 10 m/s. The red line and shaded region represent the most probable v_D and its uncertainty, respectively. See Section 3.1 for a detailed description of the analysis methods used. (For interpretation of the references to color in this figure legend, the reader is referred to the web version of this article.)

arising from Ni (and Si) substituting on an interstitial site. Thus, one may conclude that the samples investigated here are in a solid solution, implying that Ni (and Si) substitute for Fe.

Therefore, the reduction in Debye velocity of $\text{Fe}_{0.91}\text{Ni}_{0.09}$ compared with that of pure iron (as a function of density and pressure) can be understood by substituting Fe with a heavier element, such as Ni. The case for Si appears more complicated, and we return to this discussion at the end of Section 3.2.

3.2. Compressional and shear sound velocities

We combine the Debye velocities of the iron-alloys obtained from their probability distribution functions with their independently determined equations of state (Dewaele et al., 2006; Morrison et al., 2018) to constrain the compressional and shear sound velocities v_p and v_s via



$$\frac{3}{v_D^3} = \frac{1}{v_P^3} + \frac{2}{v_S^3} \quad (5)$$

and

$$\frac{K_S}{\rho} = v_P^2 - \frac{4}{3}v_S^2, \quad (6)$$

where K_S is the isentropic bulk modulus and ρ is the density of our ^{57}Fe enriched samples. K_S is related to the isothermal bulk modulus K_T via the following relation,

$$K_S = K_T(1 + \gamma\alpha T), \quad (7)$$

where γ is the Grüneisen parameter and α is the thermal expansion. For a given composition and volume, K_T is determined from existing 300 K equations of state. For bcc-Fe data, we apply the Vinet EOS for bcc-Fe reported in Morrison et al. (2018) based on compression data from Dewaele et al. (2006). For hcp-Fe, we apply the hcp-Fe EOS from

Fig. 7. Debye velocity (v_D) probability distribution functions of hcp-Fe, $\text{Fe}_{0.91}\text{Ni}_{0.09}$, and $\text{Fe}_{0.8}\text{Ni}_{0.1}\text{Si}_{0.1}$ at 300 K using a bin size of 10 m/s. The hcp-Fe data is from our re-analysis of Murphy et al. (2013), and all other data is from this study. The red line and shaded region represent the most probable v_D and its uncertainty, respectively. The uncertainty of v_D can vary noticeably depending on the NRIXS spectra and the phonon dispersions. (For interpretation of the references to color in this figure legend, the reader is referred to the web version of this article.)

Table 2
Results from NRIXS sound velocity analysis.

V	ρ^a	P	v_D^a	K_S	v_ϕ^a	v_P^a	v_S^a	G
(Å ³)	(g/cm ³)	(GPa)	(km/s)	(GPa)	(km/s)	(km/s)	(km/s)	(GPa)
bcc-Fe								
23.46(3)	8.06(1)	0	3.47(3)	168(8)	4.57(11)	5.81(9)	3.11(3)	78(1)
hcp-Fe^b								
19.66(7)	9.61(3)	30(2)	4.42(6)	312(3)	5.70(3)	7.31(5)	3.96(6)	151(4)
18.47(3)	10.25(1)	53(2)	4.61(4)	411(2)	6.33(1)	7.92(3)	4.12(4)	174(3)
17.80(3)	10.63(1)	69(3)	4.83(5)	476(1)	6.69(1)	8.35(4)	4.32(5)	198(5)
17.50(7)	10.80(2)	77(3)	4.94(2)	506(1)	6.85(1)	8.53(2)	4.41(2)	210(2)
17.10(7)	11.06(2)	90(3)	5.13(3)	558(1)	7.10(1)	8.86(2)	4.59(3)	233(3)
16.61(7)	11.38(5)	106(3)	5.21(3)	621(2)	7.39(2)	9.13(3)	4.65(3)	246(3)
16.24(7)	11.64(2)	121(3)	5.36(4)	677(2)	7.63(2)	9.42(3)	4.78(4)	266(4)
15.97(7)	11.84(2)	133(4)	5.40(8)	721(3)	7.80(2)	9.58(5)	4.82(7)	275(8)
15.61(7)	12.13(3)	151(5)	5.56(3)	786(4)	8.05(2)	9.88(3)	4.96(3)	298(4)
15.21(7)	12.43(3)	171(5)	5.68(7)	859(5)	8.31(2)	10.17(4)	5.07(6)	320(8)
bcc-Fe_{0.91}Ni_{0.09}								
23.73(2)	7.99(1)	0	3.27(2)	147(3)	4.29(5)	5.46(4)	2.93(2)	69(1)
23.38(3)	8.11(1)	1.7(1)	3.28(2)	158(2)	4.41(3)	5.56(3)	2.93(2)	70(1)
23.08(3)	8.22(1)	3.8(1)	3.31(2)	171(1)	4.56(2)	5.69(2)	2.96(2)	72(1)
22.98(3)	8.25(1)	4.5(1)	3.39(2)	175(1)	4.60(1)	5.78(2)	3.03(2)	76(1)
22.54(2)	8.41(1)	8.1(1)	3.46(1)	196(2)	4.83(2)	6.01(2)	3.09(1)	80(1)
hcp-Fe_{0.91}Ni_{0.09}								
20.59(2)	9.21(1)	18.0(1)	3.84(5)	254(3)	5.26(3)	6.58(4)	3.43(5)	109(3)
20.21(3)	9.38(1)	22.8(2)	3.94(3)	278(2)	5.44(2)	6.79(3)	3.52(3)	116(2)
19.09(6)	9.93(3)	41(1)	4.24(1)	360(1)	6.02(1)	7.44(1)	3.79(1)	142(1)
18.72(4)	10.13(2)	48(1)	4.36(4)	391(1)	6.22(1)	7.67(2)	3.89(3)	153(3)
18.07(4)	10.50(2)	63(1)	4.52(3)	456(1)	6.59(1)	8.07(2)	4.03(2)	170(2)
17.60(2)	10.77(1)	75(1)	4.60(2)	507(2)	6.86(1)	8.33(1)	4.10(2)	181(2)
17.33(3)	10.94(2)	83(1)	4.67(4)	541(2)	7.03(1)	8.51(3)	4.16(3)	189(3)
16.72(4)	11.34(3)	104(3)	4.97(4)	623(3)	7.41(2)	9.01(3)	4.43(3)	223(3)
bcc-Fe_{0.8}Ni_{0.1}Si_{0.1}								
23.38(3)	7.70(1)	0	3.21(1)	156(8)	4.49(11)	5.58(9)	2.86(1)	63(1)
22.53(3)	8.00(1)	6.5(1)	3.26(3)	191(2)	4.92(3)	5.95(3)	2.90(3)	67(1)
22.46(2)	8.02(1)	7.1(1)	3.23(3)	194(2)	4.89(3)	5.91(3)	2.87(3)	66(1)
hcp-Fe_{0.8}Ni_{0.1}Si_{0.1}								
19.90(3)	9.05(2)	27.9(3)	3.97(5)	284(3)	5.61(3)	6.94(3)	3.54(4)	114(3)
19.31(5)	9.33(2)	37.1(6)	4.16(4)	330(2)	5.95(2)	7.32(3)	3.70(3)	127(2)
19.09(6)	9.44(3)	41(1)	4.30(5)	350(2)	6.09(2)	7.53(4)	3.84(5)	139(3)
18.40(5)	9.79(3)	55(1)	4.37(4)	416(1)	6.52(1)	7.92(3)	3.90(4)	148(3)
17.83(4)	10.10(2)	69(1)	4.55(6)	480(1)	6.90(1)	8.33(3)	4.05(5)	165(4)
17.26(6)	10.44(4)	86(3)	4.68(4)	555(2)	7.30(2)	8.74(3)	4.17(4)	181(3)

^a The tabulated values for density, Debye sound velocity, bulk sound speed, compressional velocity, and shear velocity all account for ⁵⁷Fe enrichment.

^b Re-analyzed from Murphy et al. (2013).

Dewaele et al. (2006). For bcc- and hcp-Fe_{0.91}Ni_{0.09} and Fe_{0.8}Ni_{0.1}Si_{0.1}, we apply the Vinet EOSs also reported in Morrison et al. (2018). Experimental details for each equation of state are summarized in Table S2 in the Supplementary material. The EOS studies for Fe_{0.91}Ni_{0.09} and Fe_{0.8}Ni_{0.1}Si_{0.1} were conducted using samples from the same synthesis batches as the samples in this study. For samples in the bcc phase, we assume $K_S \approx K_T$. For samples in the hcp phase, we calculate K_S using our reported γ_{vib} and α_{vib} determined from the phonon DOS of each composition (see Sections 4 and 6). The shear modulus G is then calculated via

$$G = v_S^2 \rho. \quad (8)$$

The determined K_S , v_P , v_S , and G are reported in Table 2, and v_P and v_S are plotted as a function of density and pressure in Fig. 8. The density and sound velocities in Table 2 and Fig. 8 account for the ⁵⁷Fe enrichment of the samples.

From Eq. (5), one can see that the Debye velocity is mostly sensitive to shear velocity, rather than to compressional velocity. Thus, it is not surprising that the compositional trends in the shear velocity follow those observed for the Debye velocity: alloying hcp-iron with 9 at% nickel decreases the shear velocity by ~6% for a given density (or

pressure). Further alloying with 10 at% silicon has a negligible effect on the shear velocity of iron as a function of density, but trends similarly to Fe_{0.91}Ni_{0.09} with pressure (Fig. 8).

As noted previously, NRIXS measurements are better suited for constraining shear velocities, and the resulting compressional sound velocities are more strongly affected by the applied equation of state (Sturhahn and Jackson, 2007). It is therefore not surprising that for a given pressure, alloying iron with nickel has a minimal effect on compressional velocity, as their equations of state are similar in this pressure range (Morrison et al., (2018), see also Table S2). Further alloying Fe_{0.91}Ni_{0.09} with silicon also has a minimal effect on compressional velocity as a function of pressure, as differences in their equations of state compensate for their differences in density. Because Fe_{0.8}Ni_{0.1}Si_{0.1} is less dense than iron or Fe_{0.91}Ni_{0.09} when plotted as a function of density, Fe_{0.8}Ni_{0.1}Si_{0.1} has a greater v_P than that of hcp-Fe or Fe_{0.91}Ni_{0.09} (e.g., Martorell et al., 2016).

These findings suggest that nickel decreases the shear velocity of iron but not the compressional velocity of iron, while silicon has little to no effect on the compressional and shear velocities of Fe_{0.91}Ni_{0.09} for a given pressure (Fig. 8). Our findings for Fe_{0.91}Ni_{0.09} are in qualitative agreement with ab initio studies at 360 GPa and 0 K by Martorell et al. (2013a) which predict a ~5% shear velocity decrease when ~10 at%

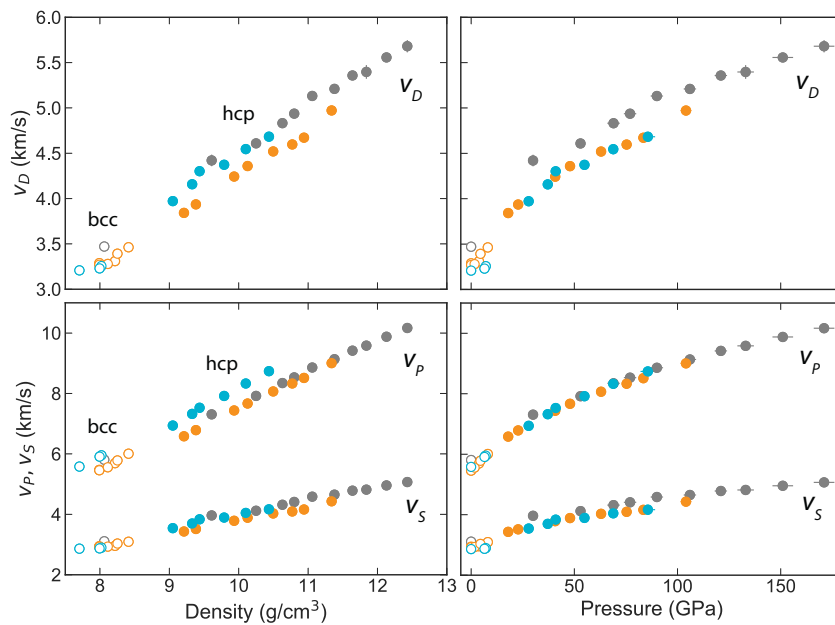


Fig. 8. Debye velocity (v_D), compressional velocity (v_p), and shear velocity (v_s) for Fe (gray), $\text{Fe}_{0.91}\text{Ni}_{0.09}$ (orange), and $\text{Fe}_{0.8}\text{Ni}_{0.1}\text{Si}_{0.1}$ (blue) as a function of density and pressure. The bcc-phase (open circles) is distinguished from the hcp-phase (filled circles). The hcp-Fe data is from our re-analysis of Murphy et al. (2013), and all other data is from this study. Sound velocity and density values account for the ^{57}Fe enrichment of the samples. (For interpretation of the references to color in this figure legend, the reader is referred to the web version of this article.)

nickel is alloyed to hcp-iron. For the case of $\text{Fe}_{0.8}\text{Ni}_{0.1}\text{Si}_{0.1}$, the combined effects of substituting a lighter element (increasing average vibrational frequency) and a heavier element (decreasing average vibrational frequency) for Fe appear to cancel one another, leading to essentially no effect on the shear velocity of pure iron as a function of density. Differences in the equation of state could then explain why v_s values of $\text{Fe}_{0.8}\text{Ni}_{0.1}\text{Si}_{0.1}$ are similar to those of $\text{Fe}_{0.91}\text{Ni}_{0.09}$ as a function of pressure. Martorell et al. (2016) studied the effects of alloying Si to Fe on the sound velocities of hcp-Fe at 360 GPa and found that hcp- $\text{Fe}_{0.9375}\text{Si}_{0.0625}$ has 2.9% lower shear velocities than hcp-Fe at 0 K. Thus, qualitatively, there is agreement in finding lower shear velocities in $\text{Fe}_{0.8}\text{Ni}_{0.1}\text{Si}_{0.1}$ compared with that of pure Fe. Although, based upon the individual studies of Martorell et al. (2013a, 2016), one may suspect that the shear velocity of $\text{Fe}_{0.8}\text{Ni}_{0.1}\text{Si}_{0.1}$ could be lower than $\text{Fe}_{0.91}\text{Ni}_{0.09}$. However, Martorell et al. (2013a, 2016) did not study the combined effects of Ni and Si. Nevertheless, Martorell et al. (2013a, 2016) show that with increasing temperature from 0 K, the effects of alloying Ni (and Si) to Fe on the compressional and shear velocities decrease and become minimal at 5500 K and 360 GPa.

3.3. Comparison with previous studies

To compare with geophysical observations and studies using samples of natural isotopic enrichment, our reported density and sound velocities can be corrected to values corresponding to natural isotopic enrichment with the following relation,

$$\rho_{\text{nat}} = \rho_{\text{enr}} (M_{\text{nat}}/M_{\text{enr}}) \quad (9)$$

and the following approximation,

$$v_{\text{nat}} = v_{\text{enr}} \sqrt{M_{\text{enr}}/M_{\text{nat}}} \quad (10)$$

where M is the molecular mass of the alloy. The subscripts *nat* and *enr* denote samples with natural isotopic enrichment and samples enriched in ^{57}Fe , respectively. Values of M_{enr} and M_{nat} are listed in Table S3.

3.4. Iron

We plot the 300 K Debye, compressional, and shear sound velocities of our bcc-Fe data and our re-analyzed hcp-Fe data from Murphy et al. (2013) in Fig. 9. We plot these as a function of pressure to compare with other NRIXS, inelastic X-ray scattering (IXS), and ultrasonic inferometry

bcc- and hcp-Fe studies, some of which do not report unit-cell volumes determined in situ. We compare to NRIXS studies by Gleason et al. (2013); Lin et al. (2005); Liu et al. (2016); Mao et al. (2001); IXS studies by Antonangeli et al. (2018); Liu et al. (2014); Mao et al. (2012); Ohtani et al. (2013); a combined NRIXS and IXS study by Mao et al. (2008); and a picosecond ultrasonic study by Decremps et al. (2014).

Unlike NRIXS studies, IXS and ultrasonic sound velocity studies do not require ^{57}Fe sample enrichment. Therefore, the plotted v_D , v_p and v_s values for bcc-Fe from this study and our re-analysis of hcp-Fe from Murphy et al. (2013) have been corrected to natural enrichment via Eq. (10). We have also corrected the reported v_D , v_p , and v_s from Gleason et al. (2013), Lin et al. (2005), Liu et al. (2016), and Mao et al. (2001) to natural isotopic enrichment using Eq. (10). As Mao et al. (2008) report v_p from samples with natural isotopic enrichment and v_D from samples enriched in ^{57}Fe , we correct their reported v_D to natural isotopic enrichment and re-calculate v_s for natural isotopic enrichment.

The v_D for hcp-Fe re-analyzed from Murphy et al. (2013) agrees well with Liu et al. (2016) that conducted experiments using a neon pressure medium and the singular value reported by Mao et al. (2008) at 50 GPa using helium as a pressure medium. These v_D trends are in reasonable agreement with the three data points reported in Gleason et al. (2013) below 85 GPa, and it is only the data point at 136 GPa (Gleason et al., 2013) that is about 2–4% higher than these aforementioned studies. The data sets of Mao et al. (2001) (no pressure medium) and Lin et al. (2005) (NaCl pressure medium) show more scatter, making it difficult to make precise comparisons.

The compressional sound velocities from IXS studies trend above those from NRIXS studies. It is therefore important to discuss the differences in the methods. In NRIXS studies, the measured quantity is the self-correlation function, where the one-phonon contribution is used to determine the phonon DOS. In the polycrystalline IXS studies of iron-alloys discussed here, the measured quantities are points along the phonon branch of the longitudinal acoustic mode (compressional wave). A fit to these points using a dispersion relation yields v_p . As discussed previously, the Debye sound velocity from NRIXS studies is obtained from the material's density and fits to the low energy region of the phonon DOS. In this study, we improve this method by determining a probability distribution function and report the most probable value given a wide range of energies and their ranges used to fit a particular spectrum. Nevertheless, there is little sensitivity to compressional wave velocity in NRIXS studies (see Sturhahn and Jackson, 2007 for a discussion of the relative sensitivities of NRIXS to v_ϕ , v_p , and v_s). The

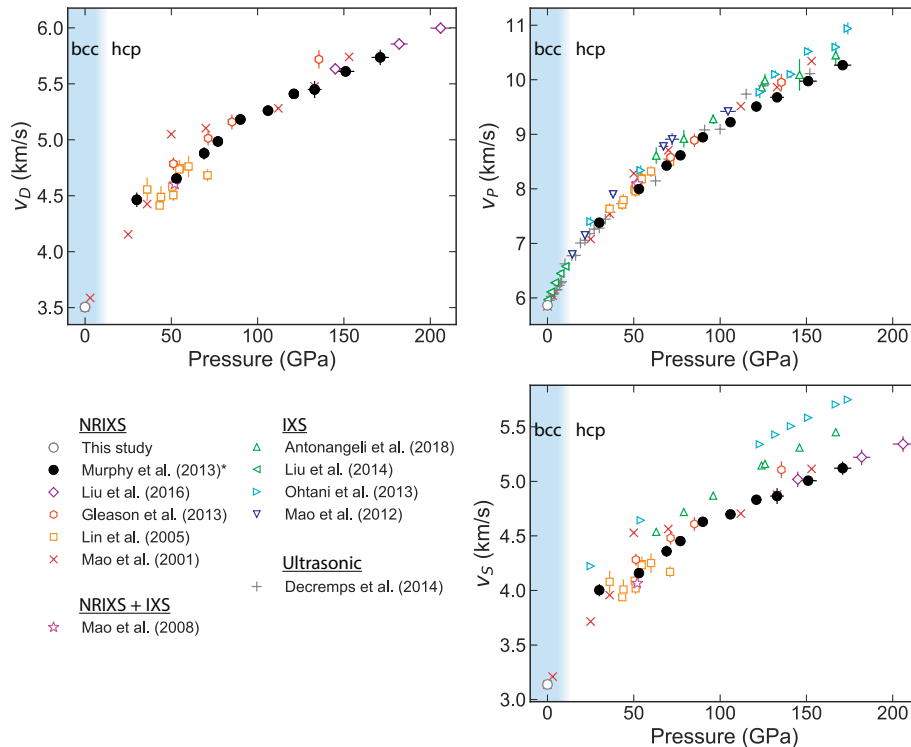


Fig. 9. A comparison of Debye (v_D), compressional (v_P), and shear (v_S) sound velocities for bcc- and hcp-Fe from NRIXS, IXS, and ultrasonic experimental studies at 300 K. Data from Murphy et al. (2013) has been re-analyzed. For NRIXS studies conducted with ^{57}Fe enriched samples, we plot sound velocities that have been corrected to those of natural enrichment via Eq. (10), except for velocities from Liu et al. (2016), where their reported natural enrichment correction was applied.

difference in v_P values between those of IXS and NRIXS studies will also be due to differences in the equations of state used, as well as the energy range used to constrain the respective sound velocities in each method. In NRIXS studies, it is common to use data starting as low as about 3 meV to determine the sound velocity.

Similar to the trends in v_D , our reported v_S for hcp-Fe agrees well with Mao et al. (2001), Lin et al. (2005), Mao et al. (2008), Liu et al. (2016), and it is only the 136 GPa data point of Gleason et al. (2013) that appears to deviate significantly from these trends. The IXS studies by Antonangeli et al. (2018) and Ohtani et al. (2013) report v_S curves based on their determined v_P and existing equations of state (Dewaele et al., 2006; Sakai et al., 2014). The v_S of Antonangeli et al. (2018) and Ohtani et al. (2013) trend respectively $\sim 5\%$ and $\sim 11\%$ above our reported v_S for hcp-Fe, which is a significant deviation. As discussed above, differences from NRIXS results can be partially attributed to the fact that the IXS studies are measuring the longitudinal acoustic branch of the phonons, not the transverse (shear) branch, and differences between the two IXS studies could be explained by different choices of equations of state used to compute v_S .

3.5. Iron-nickel

Debye, compressional, and shear sound velocities of bcc- and hcp- $\text{Fe}_{0.91}\text{Ni}_{0.09}$ are plotted in Fig. 10 and compared to results from Lin et al. (2003) for $\text{Fe}_{0.92}\text{Ni}_{0.08}$ at 300 K. Velocities from both studies have been corrected to natural enrichment via Eq. (10). The wave velocities from both studies are generally in close agreement, with the exception of the data points around 25 GPa and 50 GPa. Improved statistics due to smaller energy step sizes (0.25 meV compared to 0.5 meV), energy resolution (1.1 meV compared to 2.2 meV), and equation of state constraints from the same sample batch (Morrison et al., (2018)), along with our improved Debye velocity analysis method have allowed us to improve the constraints on hcp- $\text{Fe}_{0.91}\text{Ni}_{0.09}$ wave velocities. We robustly show that nickel decreases the shear velocity of hcp-iron. As described in Section 3.1, the reduction in shear wave velocity can be understood by substituting iron with a heavier element, such as nickel.

3.6. Iron-nickel-silicon

In Fig. 11, we compare our Debye, compressional, and shear sound velocities of bcc- and hcp- $\text{Fe}_{0.8}\text{Ni}_{0.1}\text{Si}_{0.1}$ at 300 K with existing sound velocity studies on Fe-Si and Fe-Ni-Si alloys. Previous studies include an NRIXS study on bcc- and hcp- $\text{Fe}_{0.85}\text{Si}_{0.15}$ (Lin et al., 2003); a combined NRIXS and IXS study on hcp- $\text{Fe}_{0.868}\text{Ni}_{0.086}\text{Si}_{0.046}$ (Liu et al., 2016); and IXS studies on hcp- $\text{Fe}_{0.89}\text{Ni}_{0.04}\text{Si}_{0.07}$ (Antonangeli et al., 2010), hcp- $\text{Fe}_{0.91}\text{Si}_{0.09}$ (Antonangeli et al., 2018), hcp- $\text{Fe}_{0.89}\text{Si}_{0.11}$ (Sakairi et al., 2018), bcc- and hcp- $\text{Fe}_{0.85}\text{Si}_{0.15}$ (Liu et al., 2014), and hcp- $\text{Fe}_{0.88}\text{Si}_{0.15}$ (Mao et al., 2012). Sound velocities from this study and those from Lin et al. (2003) and Liu et al. (2014) have been corrected to natural enrichment via Eq. (10). The v_S from IXS studies by Antonangeli et al. (2010, 2018) are from their reported v_S curves, which are based on their measured v_P paired with their choice of equations of state.

Our reported v_D and v_S of hcp- $\text{Fe}_{0.8}\text{Ni}_{0.1}\text{Si}_{0.1}$ are lower than those of hcp- $\text{Fe}_{0.85}\text{Si}_{0.15}$ (Lin et al., 2003). Based on our findings that nickel decreases the shear velocity of iron and that silicon has a minimal effect on the shear velocity of $\text{Fe}_{0.91}\text{Ni}_{0.09}$ for a given pressure (Fig. 8), we would expect hcp- $\text{Fe}_{0.85}\text{Si}_{0.15}$ to instead have even higher shear velocity than hcp- $\text{Fe}_{0.8}\text{Ni}_{0.1}\text{Si}_{0.1}$. Our determined v_D and v_S of hcp- $\text{Fe}_{0.8}\text{Ni}_{0.1}\text{Si}_{0.1}$ deviate from those of hcp- $\text{Fe}_{0.868}\text{Ni}_{0.086}\text{Si}_{0.046}$ (Liu et al., 2016), especially at higher pressures where hcp- $\text{Fe}_{0.868}\text{Ni}_{0.086}\text{Si}_{0.046}$ is noticeably lower than hcp- $\text{Fe}_{0.8}\text{Ni}_{0.1}\text{Si}_{0.1}$. Based on our finding that silicon has a minimal effect on the shear velocity of $\text{Fe}_{0.91}\text{Ni}_{0.09}$ for a given pressure, we would expect the values reported by Liu et al. (2016) and our study to more closely agree. Both Lin et al. (2003) and Liu et al. (2016) apply a parabolic ‘Debye-like’ phonon dispersion model to the low energy region of their phonon DOSs. Lin et al. (2003) use a fixed energy range of 3.5–14 meV for the entire pressure range. Liu et al. (2016) used $E_{min} = 3.5$ meV and varied E_{max} according to the goodness of fit χ^2 ($E_{max} = 13$ meV for 30 GPa and $E_{max} = 16.5$ meV for 133 GPa). Because alloying iron with silicon appears to decrease the parabolic ‘Debye-like’ region of the phonon DOS (see Fig. 5), a ‘Debye-like’ fit to Fe-Si and Fe-Ni-Si alloys, if extended to too large of an energy range, would produce artificially lower Debye velocities, resulting in systematically lower shear velocities. This could explain in part why the Debye and shear

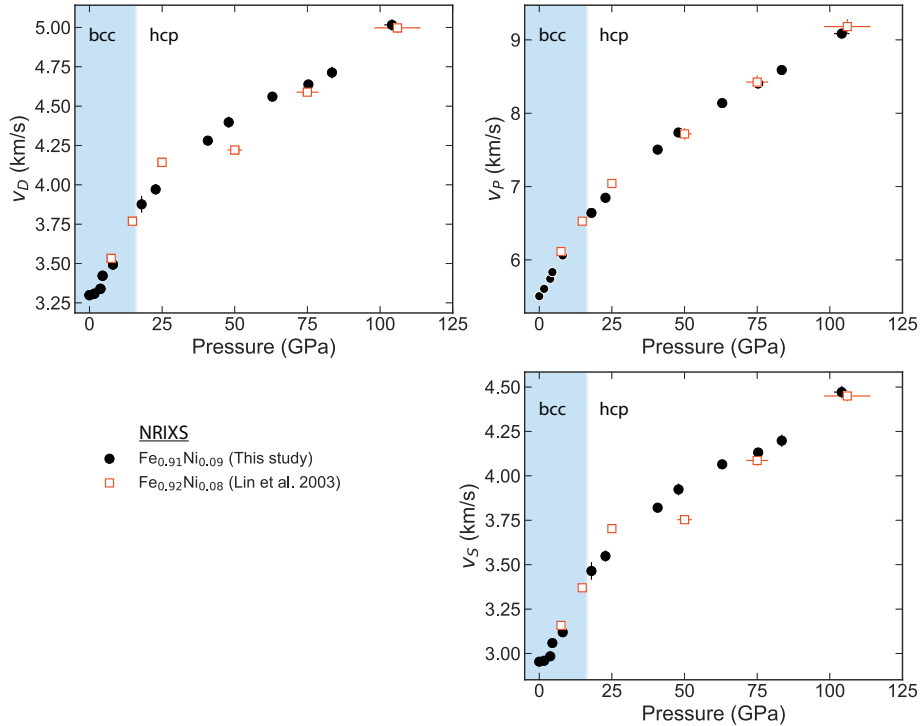


Fig. 10. A comparison of Debye (v_D), compressional (v_P), and shear (v_S) sound velocities for bcc- and hcp-Fe-Ni alloys from NRIKS experimental studies at 300 K. Both studies were conducted with ^{57}Fe enriched samples, and we plot sound velocities that have been corrected to those of natural enrichment via Eq. (10).

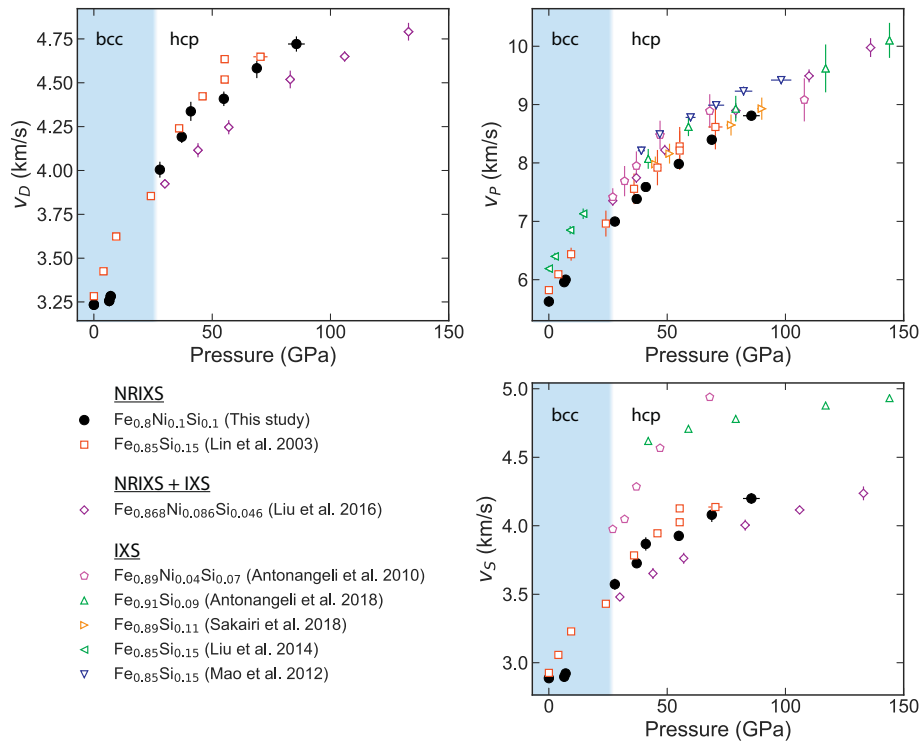


Fig. 11. A comparison of Debye (v_D), compressional (v_P), and shear (v_S) sound velocities for Fe-Si and Fe-Ni-Si alloys from NRIKS and IXS studies at 300 K. For NRIKS studies conducted with ^{57}Fe enriched samples, we plot sound velocities that have been corrected to those of natural enrichment via Eq. (10), except for velocities from Liu et al. (2016), where their reported natural enrichment correction was applied.

velocities of hcp-Fe_{0.85}Si_{0.15} (Lin et al., 2003) and hcp-Fe_{0.868}Ni_{0.086}Si_{0.046} (Liu et al., 2016) are lower than would be expected given our findings. The v_P and v_S from Lin et al. (2003) are constrained by combining v_D with existing equations of state on hcp-Fe_{0.85}Si_{0.15} from Lin (2003), although specific EOS values were not cited in Lin (2003).

When comparing with previous NRIKS studies on similar compositions, the largest deviations from our results are those of Liu et al.

(2016), with reported v_D and v_S values significantly lower than our results. As mentioned previously, v_P and v_S from our study are calculated by combining NRIKS determined v_D and in-situ unit-cell volume measurements with the Vinet hcp-Fe_{0.8}Ni_{0.1}Si_{0.1} equation of state from Morrison et al. (2018), which were all conducted with samples from the same Fe_{0.8}Ni_{0.1}Si_{0.1} synthesis batch. Liu et al. (2016) combines NRIKS constrained v_D with IXS constrained v_P to determine v_S , and pressure is determined with an equation of state for samples from their synthesis

batch. Although the sample compositions are similar between our study and Liu et al. (2016), other aspects of the data are noticeably different. The equation of state obtained in Liu et al. (2016) produces pressure differences of around +4 GPa around 50 GPa, compared to the EOS we obtain for our sample (Morrison et al., 2018); the bcc-hcp transition in Liu et al. (2016) is around 21 GPa, whereas we observe the transition around 16 GPa (Morrison et al., 2018); the NRIXS spectra are qualitatively different (the phonon modes around 25 meV produce a noticeable peak in our spectra, whereas this region is relatively flat in the spectra of Liu et al. (2016)). Further, if one uses the EOS reported in Liu et al. (2016) to compute the bulk modulus at 136 GPa, $K_{T,136\text{GPa}} = 726 \text{ GPa}$, whereas $K_{S,136\text{GPa}} = 835 \text{ GPa}$ from their reported density, v_p , and v_s at this condition, after correcting for natural enrichment. Note that the minimum energy used for constraining v_p from the IXS spectra was 30 meV (Liu et al., 2016), a value that is relatively high for use in constraining wave velocities.

The computed v_s from IXS studies by Antonangeli et al. (2010, 2018) are significantly higher than NRIXS determined v_s . Again, this could be partially attributed to the facts that the IXS studies measure the longitudinal acoustic branch of the phonons, not the transverse (shear) branch, and that the sampled data points on these phonon branches begin at relatively larger energy-transfers compared to NRIXS studies. Differences between the two IXS studies (and from the NRIXS values) could be explained by different choices of equations of state used to compute v_s .

3.7. Other light elements

We compare our reported v_D , v_p , and v_s for bcc- and hcp-Fe, Fe_{0.91}Ni_{0.09}, and Fe_{0.8}Ni_{0.1}Si_{0.1} at 300 K to the sound velocities of other candidate core compositions in Fig. 12. We include NRIXS studies on Fe₃S (Lin et al., 2004), Fe₃C (Chen et al., 2018; Gao et al., 2008), Fe₇C₃ (Chen et al., 2014), FeO, (Mg_{0.06}Fe_{0.94})O, (Mg_{0.16}Fe_{0.84})O (Wicks et al., 2017), FeH_x (Mao et al., 2004), and FeH_x (Thompson et al., 2018). We also include IXS studies on Fe₃C (Fiquet et al., 2009) and

FeH_x (Shibazaki et al., 2012). Although these compounds do not have the same crystal structures nor are they strict metallic alloys, it is informative to draw comparisons of their sound velocities with respect to discussions on iron-rich planetary cores. Note that most of the phases being compared in this section were studied using NRIXS, thus the sound velocities are plotted as reported, without a correction to natural enrichment.

When plotted as a function of pressure, the computed v_p of Fe_{0.91}Ni_{0.09} and Fe_{0.8}Ni_{0.1}Si_{0.1} from NRIXS results show negligible differences with our re-analysis of similar data for hcp-Fe (Murphy et al., 2013). The computed v_p of Fe₃S (Lin et al., 2004) trends ~4% below hcp-Fe, while the v_p of iron-hydrides (computed from NRIXS Mao et al., 2004; Thompson et al., 2018); constrained from phonon dispersion measurements (Shibazaki et al., 2012) trend above hcp-Fe. Although the v_p values of Fe₃C also trend higher than hcp-Fe (Chen et al., 2018; Fiquet et al., 2009; Gao et al., 2008), the value constrained from phonon dispersion measurements around 70 GPa (Fiquet et al., 2009) is significantly higher than the trend computed from NRIXS (Gao et al., 2008). The compressional velocities of Fe₇C₃ computed from an NRIXS study (Chen et al., 2014) shows a noticeably different dv_p/dP slope than Fe₃C. As a result, the v_p of Fe₃C falls above that of Fe above ~25 GPa, while the v_p of Fe₇C₃ falls below iron above ~70 GPa. The calculated v_p values for iron-rich (Mg,Fe)O (Wicks et al., 2017) deviate from that of hcp-Fe above ~50 GPa, as the dv_p/dP slope of (Mg,Fe)O is noticeably different from that of hcp-Fe and Fe₇C₃. At 100 GPa, the v_p of FeO is ~11% below that of hcp-Fe.

As v_D is predominately influenced by v_s rather than by v_p in NRIXS studies, the trends of v_D are similar to those of v_s in Fig. 12. Therefore we focus the following discussion on v_s . The constraints on v_s as a function of pressure suggest that silicon has a negligible effect on the v_s of hcp-Fe and that iron-hydrides (Mao et al., 2004; Shibazaki et al., 2012; Thompson et al., 2018) have a higher v_s than hcp-Fe. The elements nickel, silicon, oxygen, and carbon all appear to decrease v_s when alloyed with hcp-Fe, so it is reasonable that one or a combination of these elements may help explain the relatively low v_s of the inner core.

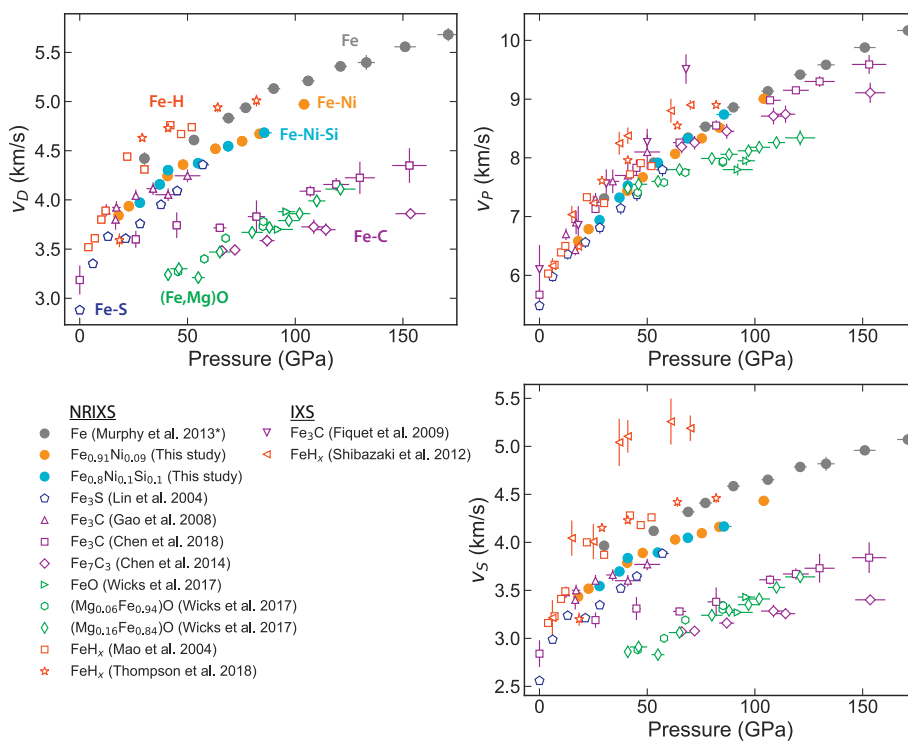


Fig. 12. Debye (v_D), compressional (v_p), and shear (v_s) sound velocities at 300 K of hcp-Fe_{0.91}Ni_{0.09} and Fe_{0.8}Ni_{0.1}Si_{0.1} and our re-analysis of hcp-Fe data from Murphy et al. (2013). We compare to other iron-light-element compositions. The sound velocities are plotted as reported without a correction to natural enrichment.

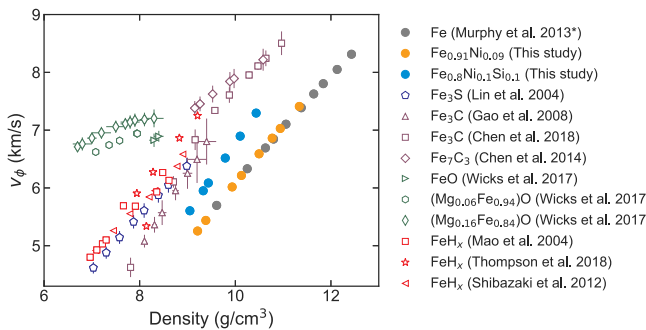


Fig. 13. Birch plot showing the bulk sound speed v_ϕ at 300 K plotted as a function of density for hcp- $\text{Fe}_{0.91}\text{Ni}_{0.09}$ and $\text{Fe}_{0.8}\text{Ni}_{0.1}\text{Si}_{0.1}$ and our re-analysis of hcp-Fe data from Murphy et al. (2013). We compare to other iron-light element compositions. The sound velocities are plotted as reported without a correction to natural enrichment.

The v_s of $\text{Fe}_{0.91}\text{Ni}_{0.09}$ trends $\sim 6.5\%$ below that of hcp-Fe at 100 GPa. Fe_3S (Lin et al., 2004) falls $\sim 10\%$ below hcp-Fe at 60 GPa, although the dv_s/dP of Fe_3S is slightly steeper than hcp-Fe, so this difference may decrease at higher pressures. At 100 GPa, the v_s of iron-rich (Mg,Fe)O (Wicks et al., 2017) is $\sim 26\%$ lower than that of hcp-Fe. The v_s of Fe_7C_3 (Chen et al., 2014) is noticeably slower than that of Fe_3C (Gao et al., 2008). From 30 to 50 GPa, the v_s of Fe_3C is $\sim 7\text{--}10\%$ slower than that of hcp-Fe, while the v_s of Fe_7C_3 is $\sim 31\%$ slower than that of hcp-Fe. The dv_s/dP slope of Fe_7C_3 is slightly lower than that of hcp-Fe, so the difference between Fe_7C_3 and hcp-Fe may increase with pressure.

We plot bulk sound speed v_ϕ for hcp-Fe, $\text{Fe}_{0.91}\text{Ni}_{0.09}$ and $\text{Fe}_{0.8}\text{Ni}_{0.1}\text{Si}_{0.1}$ at 300 K in Fig. 13. We note that the trends of hcp-Fe, $\text{Fe}_{0.91}\text{Ni}_{0.09}$, and $\text{Fe}_{0.8}\text{Ni}_{0.1}\text{Si}_{0.1}$ are all remarkably linear, suggesting the validity of Birch's law for these compositions, at least at 300 K in the pressure range investigated. We compare to v_ϕ from other NRIXS iron-light element studies, including Fe_3S (Lin et al., 2004), Fe_3C (Gao et al., 2008), Fe_7C_3 (Chen et al., 2014), FeO , $(\text{Mg}_{0.06}\text{Fe}_{0.94})\text{O}$, $(\text{Mg}_{0.16}\text{Fe}_{0.84})\text{O}$ (Wicks et al., 2017), and FeH_x (Mao et al., 2004; Thompson et al., 2018). There is noticeable scatter in the FeH_x data sets. We note that although (Mg,Fe)O exhibits a smoothly varying trend, it noticeably deviates from Birch's law. This can be explained by a spin pairing transition that occurs around a density of 8.3 g/cm^3 at 300 K for $(\text{Mg}_{0.06}\text{Fe}_{0.94})\text{O}$ (Wicks et al., 2010).

3.8. Limits to extrapolations

The extrapolation of v_p and v_s of candidate iron alloys to inner core conditions requires a fairly accurate constraint on the pressure and temperature derivatives of these quantities. Due to necessary long integration times and technique requirements for IXS and NRIXS studies, the number of data points and compression range in v_p and v_s data sets are typically much less than, for instance, in equation of state studies using X-ray diffraction. This hinders the ability to make an informed extrapolation of v_p and v_s to pressures relevant to the inner core. Furthermore, the thermal effects dv_p/dT and dv_s/dT are more poorly constrained, even for hcp-Fe. For example, a value for dv_s/dT for hcp-Fe was constrained to be $-4.6 \times 10^{-4} \text{ km}\cdot\text{s}^{-1}\cdot\text{K}^{-1}$ from a high-pressure high-temperature NRIXS study (Lin et al., 2005). A more recent constraint based on hcp-Fe ab initio constraints from Martorell et al. (2013a) gives $dv_s/dT = -3.2 \times 10^{-4} \text{ km}\cdot\text{s}^{-1}\cdot\text{K}^{-1}$.

Chen et al. (2014) suggest an inner core composed entirely of Fe_7C_3 would explain the ρ , v_p , and v_s of the inner core without invoking large sound velocity temperature effects. However, cosmochemical and iron-silicate melt partitioning studies have suggested the carbon content of the whole core is $<0.7\text{--}1 \text{ wt\%}$ (Wood et al., 2013; Zhang and Yin, 2012). An ab initio study suggested the density of Fe_7C_3 was too low to be a substantial component of the inner core (Li et al., 2016), and, in

the analysis of equations of state and seismic observations, Morrison et al. (2018) find a carbon content of $<1 \text{ wt\%}$. FeO and iron-rich (Mg,Fe)O also have a low v_s compared to that of hcp-Fe, suggesting a large oxygen content could explain the low v_s of the inner core. However, solid-liquid iron partitioning studies have suggested oxygen is largely incompatible in the inner core (Alfè et al., 2002, 2007). Additionally, Morrison et al. (2018) found the bulk sound speed of FeO limited the oxygen content of the inner core to 2 wt%. It is of course recognized that these constraints were obtained from mixing end-member components which do not have the same crystal structures, and thus more realistic candidate core-forming alloys must be examined in the future. Nevertheless, constraining the effect of large compression and very high temperatures ($\sim 4000\text{--}5000 \text{ K}$) on the sound velocities of realistic iron-nickel alloys, combined with tighter seismic constraints, will be essential to take the next steps in constraining inner core composition using mineral elasticity data.

4. Vibrational Grüneisen parameter

The vibrational component of the Grüneisen parameter γ_{vib} for a given phonon mode can be defined as the volume dependence of energy of that phonon mode,

$$\gamma_{vib} = -\frac{\partial \ln \omega}{\partial \ln V} = -\frac{\partial \ln E}{\partial \ln V}, \quad (11)$$

where ω is the frequency corresponding to the given phonon mode, and E is the corresponding energy. As we have measured the phonon DOS for each composition as a function of volume, we can evaluate constraints for the vibrational Grüneisen parameter, such as using a phonon DOS scaling relation (Murphy et al., 2011a). We plot our phonon DOSs for each hcp phase in Fig. 14. Upon visual inspection, the phonon DOSs for a given composition appear to be related by a single scaling parameter. For a given hcp phase, we scale a single phonon DOS $D(E, V_i)$ to all other phonon DOSs $D(E, V)$ using the relation

$$D(E, V) = \xi(V, V_i) D[\xi(V, V_i) E, V_i], \quad (12)$$

where V_i is the volume of the reference phonon DOS, V is the volume to which the reference phonon DOS is scaled, $\xi(V, V_i)$ is an energy independent scaling parameter, and $\xi(V, V_i) = 1$ when $V = V_i$. For hcp- $\text{Fe}_{0.91}\text{Ni}_{0.09}$, we compare the measured phonon DOSs to the scaled phonon DOS measured at $V_i = 18.72 \pm 0.04 \text{ \AA}^3$ ($P = 48 \pm 1 \text{ GPa}$) in the left panel of Fig. 14. Similarly, for hcp- $\text{Fe}_{0.8}\text{Ni}_{0.1}\text{Si}_{0.1}$, we compare the measured phonon DOSs to the scaled phonon DOS measured at $V_i = 19.09 \pm 0.06 \text{ \AA}^3$ ($P = 41 \pm 1 \text{ GPa}$) in the middle panel of Fig. 14. For our re-analysis of hcp-Fe, we compare the measured phonon DOSs to the scaled phonon DOS measured at $V_i = 17.10 \pm 0.07 \text{ \AA}^3$ ($P = 90 \pm 3 \text{ GPa}$) in the right panel of Fig. 14.

For a given hcp phase, we apply Eq. (12) to scale a reference phonon DOS $D(E, V_i)$ to all other phonon DOSs $D(E, V)$ using a linear least squares regression, thereby obtaining a scaling parameter corresponding to each pair of phonon DOSs. We repeat this process with the other phonon DOS acting as the reference to obtain a total of $7 \times 8 = 56$ scaling parameters for hcp- $\text{Fe}_{0.91}\text{Ni}_{0.09}$, $5 \times 6 = 30$ scaling parameters for hcp- $\text{Fe}_{0.8}\text{Ni}_{0.1}\text{Si}_{0.1}$, and $9 \times 10 = 90$ scaling parameters for hcp-Fe. These scaling parameters are plotted as a function of V/V_i in Fig. S3. The near-linear trend of the scaling parameter ξ with respect to V/V_i demonstrates the applicability of the scaling law in Eq. (12).

We combine a rephrasing of Eq. (11),

$$\gamma_{vib} = -\frac{\partial \ln \xi(V, V_i)}{\partial \ln V_i}, \quad (13)$$

with the commonly applied empirical relation,

$$\gamma_{vib} = \gamma_{vib,i} \left(\frac{V}{V_i} \right)^q, \quad (14)$$

where q is a fitting parameter, and the subscript i refers to a reference

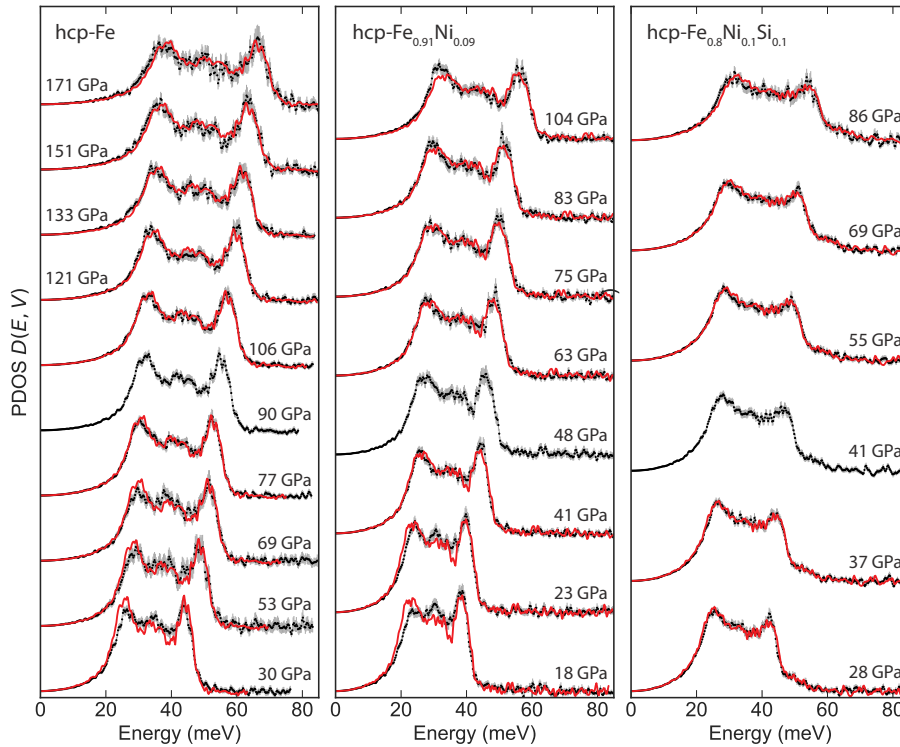


Fig. 14. Examples of scaled phonon DOSs (red) compared to measured phonon DOS (black with gray error bars) for hcp-structured $\text{Fe}_{0.91}\text{Ni}_{0.09}$, $\text{Fe}_{0.8}\text{Ni}_{0.1}\text{Si}_{0.1}$, and our re-analysis of Fe data from Murphy et al. (2011a). The hcp- $\text{Fe}_{0.91}\text{Ni}_{0.09}$ phonon DOS at 48 GPa and the hcp- $\text{Fe}_{0.8}\text{Ni}_{0.1}\text{Si}_{0.1}$ phonon DOS at 41 GPa are scaled to each compression point according to Eq. (12). Similarly, our re-analyzed phonon DOS of hcp-Fe from Murphy et al. (2013) at 90 GPa is scaled to each compression point following the same method. (For interpretation of the references to color in this figure legend, the reader is referred to the web version of this article.)

phonon DOS. Combining Eqs. (13) and (14) and integrating yields

$$\xi(V, V_i) = \exp \left\{ \frac{\gamma_{vib,i}}{q} \left[\left(\frac{V}{V_i} \right)^q - 1 \right] \right\}, \quad (15)$$

where $q \neq 0$. Substituting an analogous relation to Eq. (14),

$$\gamma_{vib,i} = \gamma_{vib,0} \left(\frac{V_i}{V_0} \right)^q, \quad (16)$$

into Eq. (15) yields

$$\xi(V, V_i) = \exp \left\{ \frac{\gamma_{vib,0}}{q} \left(\frac{V_i}{V_0} \right)^q \left[\left(\frac{V}{V_i} \right)^q - 1 \right] \right\}, \quad (17)$$

where ξ is the scaling parameter as a function of volume V and reference volume V_i . V_0 is the volume at 0 GPa, as determined with an equation of state (Morrison et al., 2018). The vibrational Grüneisen parameter at 0 GPa, $\gamma_{vib,0}$, and q are fitting parameters. We applied Eq. (17) to the scaling parameters in Fig. S3 using a linear least squares regression to determine $\gamma_{vib,0}$ and q . Then Eq. (16) was applied to determine the vibrational Grüneisen parameter as a function of volume V_i .

We applied a grid search to the regression of Eq. (17), and we found the scaling parameter values shown in Fig. S3 do not constrain q . Therefore, we fix q at the commonly assumed value of 1, and obtain values of $\gamma_{vib,0} = 2.04 \pm 0.01$ for hcp-Fe, $\gamma_{vib,0} = 2.07 \pm 0.02$ for hcp- $\text{Fe}_{0.91}\text{Ni}_{0.09}$, and $\gamma_{vib,0} = 2.03 \pm 0.05$ for hcp- $\text{Fe}_{0.8}\text{Ni}_{0.1}\text{Si}_{0.1}$ (listed in Table 3). The resulting vibrational Grüneisen parameters are plotted as lines with shaded uncertainties in Fig. 15.

To test the robustness and validity of the above method, we approximate the vibrational Grüneisen parameter with a second method outlined in the supplemental material. While this second method is a coarse approximation for $\gamma_{vib,i}$, we note that it does not rely on the application of the empirical relation in Eq. (14), or a linear least squares fit, or on fixing the fitting parameter q . Therefore, it serves as a check of the validity of Eq. (17). Both methods of determining $\gamma_{vib,i}$ agree well within error bars within the measured volume region (Fig. S9).

The γ_{vib} for hcp- $\text{Fe}_{0.91}\text{Ni}_{0.09}$ and our re-analysis of hcp-Fe data from

Table 3

Grüneisen parameters from this study, Fei et al., (2016); Murphy et al., (2011a).

Phase	Study	$\gamma_{vib,0}$	q
hcp-Fe	This study	2.04(1)	1.0 (fixed)
hcp- $\text{Fe}_{0.91}\text{Ni}_{0.09}$	This study	2.07(2)	1.0 (fixed)
hcp- $\text{Fe}_{0.8}\text{Ni}_{0.1}\text{Si}_{0.1}$	This study	2.03(5)	1.0 (fixed)
hcp-Fe	(Murphy et al., 2011a)	2.0(1)	1.0(2)
hcp-Fe	(Fei et al., 2016)	1.74	0.78

Murphy et al. (2011a) are in close agreement and nearly indistinguishable within our reported error bars, and those for $\text{Fe}_{0.8}\text{Ni}_{0.1}\text{Si}_{0.1}$ trend lower (Fig. 15). We compare to previously reported values of γ_{vib} for hcp-Fe. Ab initio calculations by Sha and Cohen (2010) computed at 500 K are similar to our results, although the slope of γ_{vib} with respect to volume is noticeably different. The γ_{vib} reported by Dewaele et al. (2006) is determined with shock-wave and 300 K static compression XRD data and is in close agreement with our results. Merkel et al. (2000) estimate γ_{vib} with Raman spectroscopy at 300 K, and Dubrovinsky et al. (2000) estimate γ_{vib} with static compression XRD data.

Fei et al. (2016) calculate γ_{vib} from the results of Murphy et al. (2011a), much as we do in this study. In Fig. 16, we compare γ_{vib} reported in Fei et al. (2016), Murphy et al. (2011a), and our study, which all use the same NRIXS hcp-Fe data set from Murphy et al. (2011a). We plot our γ_{vib} results for hcp-Fe calculated using Eq. (17). Note that each study applies the same empirical constraint of Eq. (14). Our analyses are internally consistent and in close agreement with published results from Murphy et al. (2011a) with $q = 1$. Small differences between our analysis using Eq. (17) and reported values from Murphy et al. (2011a) are likely due to our exclusion of the NRIXS data set at 36 GPa. However, our results of γ_{vib} trend significantly higher than the trend reported in Fei et al. (2016).

We investigate the difference between our γ_{vib} analysis and that of Fei et al. (2016), and we estimate the effect of this difference on the extrapolation of an EOS to inner core conditions. We apply Eq. (15) to the γ_{vib} of Fei et al. (2016), and we compare the resulting scaled phonon

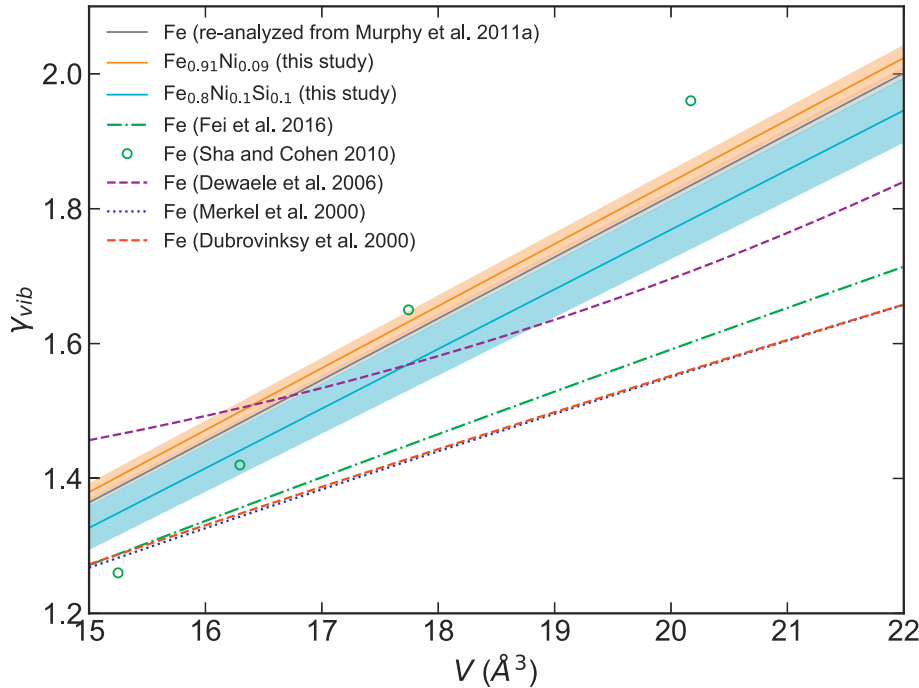


Fig. 15. Vibrational Grüneisen parameter γ_{vib} for hcp- $\text{Fe}_{0.91}\text{Ni}_{0.09}$, $\text{Fe}_{0.8}\text{Ni}_{0.1}\text{Si}_{0.1}$, and Fe calculated with Eq. (17) compared γ_{vib} for hcp-Fe determined from results of NRIXS measurements by Murphy et al. (2011a) re-analyzed by Fei et al. (2016), ab initio calculations at 500 K (Sha and Cohen, 2010), shock-wave and 300 K static compression XRD data (Dewaele et al., 2006), static compression Raman spectroscopy at 300 K (Merkel et al., 2000), and static compression XRD data (Dubrovinsky et al., 2000).

DOS to ours in Fig. 17 and Figs. S4 and S5 in the Supplementary material. Fig. 17 illustrates the scaling using the 30 GPa phonon DOS, and Figs. S4 and S5 illustrate the scaling using the 90 and 171 GPa phonon DOS, respectively. The scaling fit in this study weights the phonon modes roughly evenly, whereas the scaling fit in Fei et al. (2016) preferentially fits the lower energy region of the phonon DOS. This is particularly evident in Figs. 17 and S5 in the Supplementary material. The γ_{vib} from Fei et al. (2016) appears to be closer to the Debye Grüneisen parameter, defined as

$$\gamma_D = \frac{1}{3} - \frac{V}{v_D} \left(\frac{v_D}{V} \right)_T. \quad (18)$$

This is also supported by the close agreement between the γ_{vib} from Fei et al. (2016) and the γ_D from Murphy et al. (2011a).

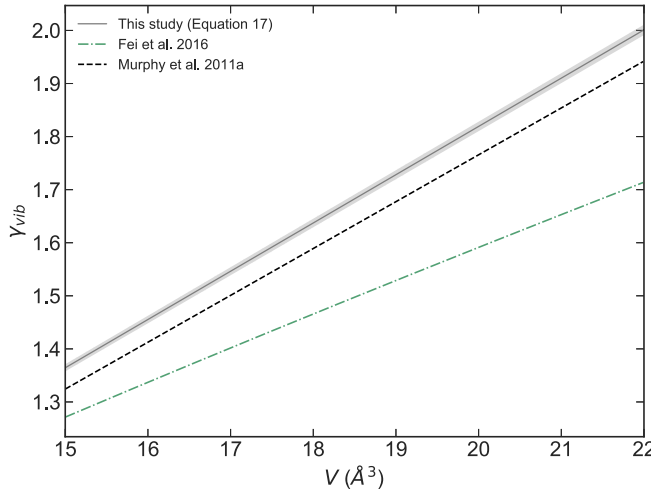


Fig. 16. Various reported γ_{vib} determined from the hcp-Fe NRIXS data reported in Murphy et al. (2011a). Our analysis using Eq. (17) and $q = 1$ are internally consistent and in agreement with published results from Murphy et al. (2011a) with $q = 1$. Our analysis is not in agreement with results from Fei et al. (2016).

We estimate the impact of γ_{vib} from Fei et al. (2016), Murphy et al. (2011a), and this study on the isothermal EOS extrapolation to inner core conditions. We extrapolate the 300 K hcp-iron EOS from Dewaele et al. (2006) to 5500 K using the methods described in Morrison et al. (2018). We apply $\Theta_0 = 417$ K and each of the γ_{vib} from Fei et al. (2016), Murphy et al. (2011a) and this study. The resulting density, bulk modulus, and bulk sound speed are compared in Fig. 18. The bars to the right represent the estimated uncertainty as reported in Morrison et al. (2018), where contributions from electronic or anharmonic contributions to thermal pressure are excluded in order to isolate the effect of different γ_{vib} and q values used. The seismic model AK135-F is plotted for reference (Kennett et al., 1995) with uncertainties for ρ (2%), K_S (2.3%), and v_ϕ (0.6%) (Deuss, 2008; Masters and Gubbins, 2003).

The γ_{vib} from Fei et al. (2016); Murphy et al. (2011a), and this study produces densities, bulk moduli, and bulk sound speed at 5500 K and inner core pressures that agree within 0.5%. In comparison to the current equation of state uncertainty and seismic uncertainty, this difference is negligible. This is before taking into account the contributions from electronic or anharmonic terms to thermal pressure. Morrison et al. (2018) estimated the electronic and anharmonic contributions to thermal pressure with theoretical calculations from Dewaele et al. (2006) and found a combined $P_{el} + P_{ahn}$ of 14.5 GPa at 5500 K. At 5500 K and 13.7 g/cm³ density, the formulation from Fei et al. (2016) estimates $P_{el} + P_{ahn} = 14.8$ GPa, in close agreement with Dewaele et al. (2006). Therefore, adding electronic and anharmonic contributions to thermal pressure to Fig. 18 would not noticeably change the difference between the three compared thermal equations of state for hcp-iron.

Morrison et al. (2018) applied the γ_{vib} from Murphy et al. (2011a) and $\Theta_0 = 417$ K (Dewaele et al., 2006) to isothermal equations of state of hcp- $\text{Fe}_{0.91}\text{Ni}_{0.09}$ and $\text{Fe}_{0.8}\text{Ni}_{0.1}\text{Si}_{0.1}$ to determine thermal equations of state. They then reported the corresponding ρ , K_S , and v_ϕ . We find the differences between the γ_{vib} of hcp-Fe, $\text{Fe}_{0.91}\text{Ni}_{0.09}$, and $\text{Fe}_{0.8}\text{Ni}_{0.1}\text{Si}_{0.1}$ to be within mutual uncertainty, and our re-analysis of γ_{vib} of hcp-Fe is in close agreement with that of Murphy et al. (2011a). Therefore, we conclude that our application of the γ_{vib} of hcp-Fe from Murphy et al. (2011a) to hcp- $\text{Fe}_{0.91}\text{Ni}_{0.09}$ and $\text{Fe}_{0.8}\text{Ni}_{0.1}\text{Si}_{0.1}$ in Morrison et al. (2018) is a reasonable approximation.

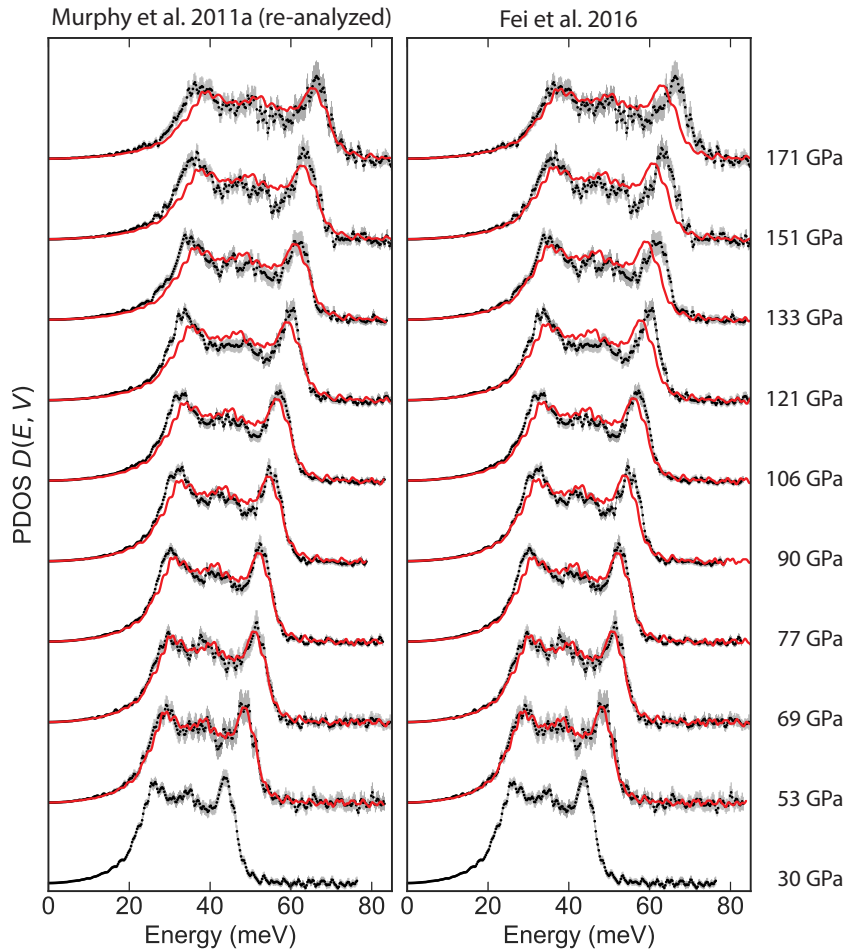


Fig. 17. Scaled phonon DOSs (red) compared to measured phonon DOS (black with gray error bars) for hcp-structured Fe. The hcp-Fe phonon DOS at 30 GPa is scaled to each compression point according to Eq. (12). On the left is our analysis of Murphy et al. (2011a), and on the right is the phonon DOS scaling calculated from γ_{vib} to each compression point according to Eq. (12). (For interpretation of the references to color in this figure legend, the reader is referred to the web version of this article.)

5. Vibrational free energy

In Section 4, we determined the vibrational Grüneisen parameter for the suite of iron-alloys investigated here from a scaling approach to the measured phonon DOS. We showed the application of the vibrational Grüneisen parameter to estimates of hcp-iron's thermoelastic properties at inner core conditions using Mie-Grüneisen-Debye thermal equation of state. Another approach to estimating the thermal properties of a solid is to evaluate the volume dependence of the vibrational free energy of the material, as outlined in Murphy et al. (2011a, 2011b, 2013).

The harmonic (h) vibrational free energy F_{vib}^h is accessible from the phonon DOS with

$$F_{vib}^h = \frac{1}{\beta} \int \ln \left(2 \sinh \frac{\beta E}{2} \right) D(E, V) dE, \quad (19)$$

where $\beta = (k_B T)^{-1}$. When combined with the electronic and anharmonic components of pressure, P_{el} and P_{vib}^{anh} , this yields the total thermal pressure P_{th} ,

$$P_{th} = P_{vib}^h + P_{el} + P_{vib}^{anh} = - \left(\frac{\partial F_{vib}^h}{\partial V} \right)_T - \left(\frac{\partial F_{el}}{\partial V} \right)_T - \left(\frac{\partial F_{vib}^{anh}}{\partial V} \right)_T. \quad (20)$$

Constraints on the thermal properties of hcp-iron have also come from shock-compression experiments using the thermodynamic Grüneisen parameter and Mie-Grüneisen theory (Brown and McQueen, 1986; Jeanloz, 1979) and theoretical studies (Alfè et al., 2001; Bouchet et al., 2013; Sha and Cohen, 2010; Stixrude et al., 1997; Vočadlo et al.,

2000; Wasserman et al., 1996), in addition to those discussed in Section 4. By comparison, the thermal pressure of iron-nickel and iron-silicon alloys has received little attention. Zhang et al. (2014) investigate the thermal pressure of iron-nickel-silicon alloys with shock compression, and Côté et al. (2010, 2012) apply theoretical calculations to study the thermal pressure of iron-silicon and iron-nickel alloys, respectively. Here, we apply the methods of (Murphy et al., 2011b) to $Fe_{0.91}Ni_{0.09}$ and $Fe_{0.8}Ni_{0.1}Si_{0.1}$. For consistency, we also re-analyze NRIXS data from Murphy et al. (2011a) to ensure a systematic comparison of the alloys.

The vibrational free energy F_{vib}^h of $Fe_{0.91}Ni_{0.09}$, $Fe_{0.8}Ni_{0.1}Si_{0.1}$, and Fe at 300 K is plotted in Fig. S6, and we fit empirical second-order polynomials to the F_{vib}^h of the hcp phases to calculate the derivative $(\partial F_{vib}^h / \partial V)_T$. The polynomials are listed in Fig. S6, where volume V is in \AA^3 and F_{vib}^h is in meV/atom. We find the curvature of F_{vib}^h for hcp- $Fe_{0.8}Ni_{0.1}Si_{0.1}$ is poorly constrained due to the smaller compression range explored for the Fe-Ni-Si alloy. We find for hcp-Fe that $P_{vib}^h = -0.29V + 7.5$, for hcp- $Fe_{0.91}Ni_{0.09}$ that $P_{vib}^h = -0.21V + 6.2$, and for that hcp- $Fe_{0.8}Ni_{0.1}Si_{0.1}$ $P_{vib}^h = -0.07V + 3.6$, where V is in \AA^3 and P_{vib}^h has been converted to units of GPa. The resulting P_{vib}^h are plotted in Fig. S7, and the F_{vib}^h and corresponding P_{vib}^h for each hcp volume can be found in Table 4.

As can be seen in Eq. (19), F_{vib}^h is directly proportional to temperature. Therefore, our 300 K data can be used to inform the temperature dependence of the harmonic P_{vib}^h with the following relation:

$$P_{vib}^h(V, T) = \left(\frac{T}{300 \text{ K}} \right) P_{vib}^h(V, 300 \text{ K}). \quad (21)$$

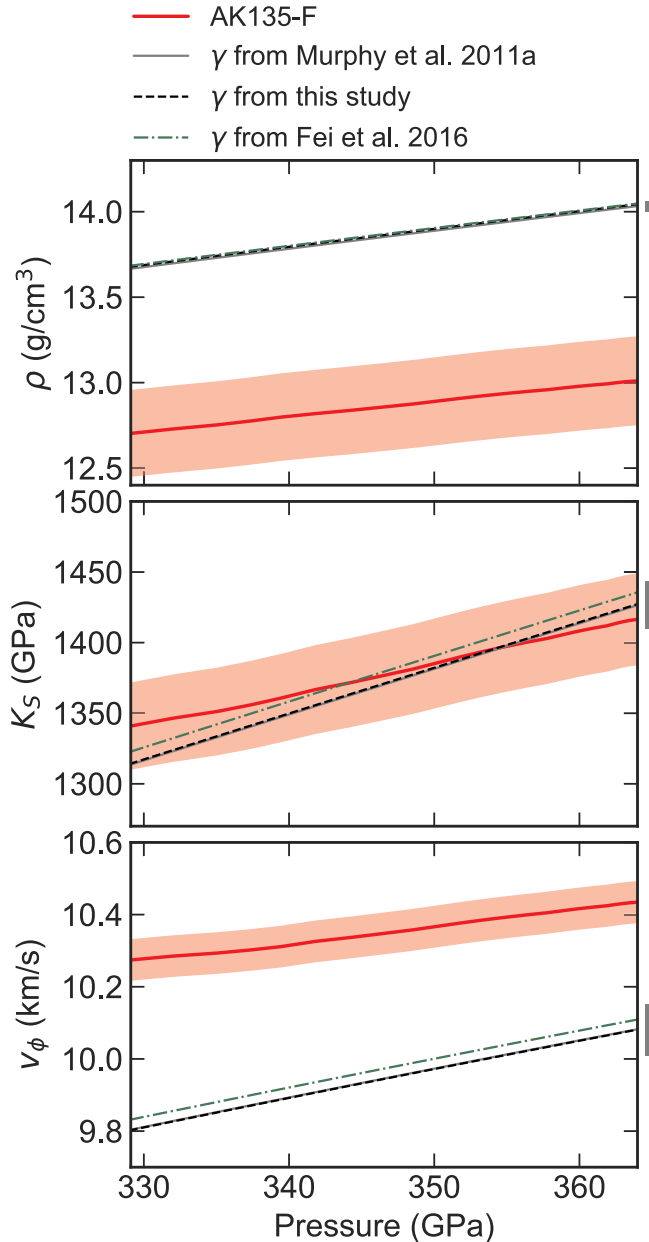


Fig. 18. Thermal EOSs for hcp-Fe (Dewaele et al., 2006) are extrapolated to inner core conditions to calculate density ρ , adiabatic bulk modulus K_s , and bulk sound speed v_ϕ as a function of pressure at 5500 K (see text for details). Estimated electronic and anharmonic contributions to thermal pressure are not included. Bars (right) represent uncertainty due to EOS parameters for hcp-Fe. We compare to the seismic model AK135-F (red line) (Kennett et al., 1995) with estimated uncertainties for ρ (2%), K_s (2.3%), and v_ϕ (0.6%) (Deuss, 2008; Masters and Gubbins, 2003). (For interpretation of the references to color in this figure legend, the reader is referred to the web version of this article.)

We plot the temperature dependent harmonic P_{vib}^h in Fig. 19, and compare to the harmonic P_{vib}^h calculated by (Alfè et al., 2001). We note that the slope of P_{vib}^h with volume of hcp-Fe is steeper than that previously published by (Murphy et al., 2011b), due in part to our exclusion of the NRIXS data at 36 GPa, which had much lower statistical quality compared with the other compression points in the same data set. Our re-analysis of P_{vib}^h for hcp-Fe deviates significantly, especially at lower volumes (higher pressures) from theoretical calculations reported in (Alfè et al., 2001) (Fig. 19). The P_{vib}^h for hcp-Fe_{0.91}Ni_{0.09} is nearly indistinguishable from that of hcp-Fe. The slope of P_{vib}^h for hcp-Fe_{0.8}Ni_{0.1}Si_{0.1} is more shallow than that of hcp-Fe or Fe_{0.91}Ni_{0.09},

although we note the slope of hcp-Fe_{0.8}Ni_{0.1}Si_{0.1} is not as well constrained due to the smaller compression range explored.

Our above discussion does not include the anharmonic P_{vib}^{anh} and the electronic P_{el} contributions to the thermal pressure P_{th} , as the phonon DOSs at 300 K for these alloys are insensitive to these components. The P_{vib}^{anh} and P_{el} of iron alloys are not well constrained by experimental data. Murphy et al. (2011b), Sakai et al. (2014) used the P_{vib}^{anh} and P_{el} of hcp-Fe reported in Dewaele et al. (2006). These values are based on hcp-Fe ab initio calculations by (Alfè et al., 2001) and use the P_{vib}^h and P_{el} formulation from Dorogokupets and Oganov (2006). As similar ab initio calculations are not available for hcp-Fe_{0.91}Ni_{0.09} and Fe_{0.8}Ni_{0.1}Si_{0.1}, we applied the hcp-Fe P_{vib}^h and P_{el} terms from Dewaele et al. (2006) to each of our hcp-structured compositions to estimate P_{th} . For modeling metallic materials at very high temperatures, the electronic term becomes significant. For example, at 104 GPa and 5500 K, the contributions from P_{vib}^h , P_{vib}^{anh} , and P_{el} for hcp-Fe_{0.91}Ni_{0.09} are as follows: 49 GPa, 3 GPa, and 13 GPa, respectively. The estimated contributions of P_{vib}^h , P_{vib}^{anh} , and P_{el} for hcp-Fe_{0.91}Ni_{0.09}, Fe_{0.8}Ni_{0.1}Si_{0.1}, and Fe at 5500 K are tabulated in Table 4, and the corresponding total thermal pressures P_{th} for 300 K, 2000 K, 4000 K, and 5500 K are plotted in Fig. S8.

6. Vibrational entropy and thermal expansion

The volumetric thermal expansion coefficient α_{vib} can be obtained from the volume dependence of the vibrational entropy and the isothermal bulk modulus. The vibrational entropy per ⁵⁷Fe resonant atom, S_{vib} , is accessible via the phonon DOS,

$$S_{vib} = \frac{k_B\beta}{2} \int E \coth \frac{\beta E}{2} D(E, V) dE - k_B \int \ln \left(2 \sinh \frac{\beta E}{2} \right) D(E, V) dE. \quad (22)$$

The S_{vib} for bcc- and hcp-Fe_{0.91}Ni_{0.09}, Fe_{0.8}Ni_{0.1}Si_{0.1}, and Fe are plotted in Fig. S11.

The derivative of S_{vib} with respect to volume is related to volumetric α_{vib} with

$$\alpha_{vib} = \frac{1}{K_T} \left(\frac{\partial S_{vib}}{\partial V} \right)_T, \quad (23)$$

where K_T is the isothermal bulk modulus, accessible with equations of state (EOSs). For hcp-Fe_{0.91}Ni_{0.09} and Fe_{0.8}Ni_{0.1}Si_{0.1}, we use the corresponding Vinet EOSs from Morrison et al. (2018). For hcp-Fe, we use the Vinet EOS from Dewaele et al. (2006). The EOS experimental conditions and parameters are listed in Table S2. To calculate $(\partial S_{vib}/\partial V)_T$, we apply linear fits to the hcp data. These fits and their corresponding equations are displayed in Fig. S11. Our resulting α_{vib} for the hcp phases at 300 K are plotted in Fig. 20 and tabulated in Table S5. The α_{vib} of hcp-Fe and Fe_{0.91}Ni_{0.09} are in close agreement, while Fe_{0.8}Ni_{0.1}Si_{0.1} has a slightly higher thermal expansion at large volumes. At smaller volumes, α_{vib} of Fe_{0.8}Ni_{0.1}Si_{0.1} seems to approach that of hcp-Fe and Fe_{0.91}Ni_{0.09}.

7. Conclusions

We performed high pressure nuclear resonant inelastic X-ray scattering (NRIXS) measurements on bcc- and hcp-Fe_{0.91}Ni_{0.09} and Fe_{0.8}Ni_{0.1}Si_{0.1} at 300 K with in situ X-ray diffraction. From these data, we determine the partial phonon density of states for each composition. To ensure a systematic comparison to pure iron, we re-analyze the hcp-iron NRIXS data presented in Murphy et al. (2011a, 2011b, 2013) using the same methods used to analyze our Fe_{0.91}Ni_{0.09} and Fe_{0.8}Ni_{0.1}Si_{0.1} data sets.

We demonstrate a new method of determining the Debye sound velocity from the low energy region of the phonon DOS. This method applies the corrected Akaike Information Criterion and uses a binning

Table 4

Thermal pressure components for hcp phases: harmonic vibrational free energy (F_{vib}^h) and pressure (P_{vib}^h), anharmonic (P_{vib}^{anh}) and electronic pressures (P_{el}).

V	At 300 K			At 5500 K			
	P	F_{vib}^h	P_{vib}^h	P_{vib}^h	P_{vib}^{anh}	P_{el}^b	P_{th}
(Å ³)	(GPa)	(meV/atom)	(GPa)	(GPa)	(GPa)	(GPa)	(GPa)
hcp-Fe^a							
19.66(7)	30(2)	21.6(4)	1.83(9)	33.5(16)	3.4	13.9	50.8
18.47(3)	53(2)	29.4(10)	2.17(5)	39.7(9)	3.3	13.7	56.7
17.80(3)	69(3)	34.3(8)	2.36(3)	43.3(5)	3.2	13.5	60.0
17.50(7)	77(3)	35.8(5)	2.45(3)	44.8(5)	3.1	13.4	61.3
17.10(7)	90(3)	39.3(5)	2.56(3)	47.0(5)	3.1	13.3	63.4
16.61(7)	106(3)	42.8(5)	2.70(4)	49.5(7)	3.0	13.2	65.7
16.24(7)	121(3)	46.6(7)	2.81(5)	51.5(9)	2.9	13.1	67.5
15.97(7)	133(4)	49.1(8)	2.89(6)	52.9(10)	2.9	13.0	68.8
15.61(7)	151(5)	52.0(10)	2.99(7)	54.8(12)	2.8	12.9	70.5
15.21(7)	171(5)	56.1(12)	3.10(8)	56.9(15)	2.8	12.8	72.5
hcp-Fe_{0.91}Ni_{0.09}							
20.59(2)	18.0(1)	12.0(6)	1.89(22)	34.7(40)	3.6	14.1	52.4
20.21(3)	22.8(2)	13.3(7)	1.97(18)	36.1(33)	3.5	14.0	53.6
19.09(6)	41(1)	21.7(7)	2.20(8)	40.4(14)	3.3	13.7	57.4
18.72(4)	48(1)	24.4(8)	2.28(6)	41.8(11)	3.3	13.7	58.8
18.07(4)	63(1)	28.7(8)	2.41(10)	44.3(18)	3.2	13.5	61.0
17.60(2)	75(1)	31.2(8)	2.51(14)	46.0(26)	3.1	13.4	62.5
17.33(3)	83(1)	34.1(8)	2.57(17)	47.0(31)	3.1	13.3	63.4
16.72(4)	104(3)	39.9(8)	2.69(23)	49.4(43)	3.0	13.1	65.5
hcp-Fe_{0.8}Ni_{0.1}Si_{0.1}							
19.90(3)	27.9(3)	18.3(5)	2.30(49)	42.2(91)	3.3	13.6	59.1
19.31(5)	37.1(6)	21.9(5)	2.34(30)	42.9(54)	3.2	13.4	59.5
19.09(6)	41(1)	25.2(5)	2.35(23)	43.1(42)	3.2	13.4	59.7
18.40(5)	55(1)	29.6(8)	2.40(15)	44.0(27)	3.1	13.2	60.3
17.83(4)	69(1)	32.7(10)	2.44(29)	44.7(54)	3.0	13.1	60.8
17.26(6)	86(3)	38.4(10)	2.47(48)	45.3(89)	2.9	12.9	61.1

^a Re-analyzed from Murphy et al. (2011a, 2011b, 2013).

^b From Dewaele et al. (2006).

of many possible fit ranges to determine a probability distribution function of the Debye sound velocity. Unlike previous methods, this method does not depend on picking an energy fit range for the phonon DOS, and it provides an improved estimate on the Debye sound velocity uncertainty. Using this new method, Debye sound velocities were

determined for bcc- and hcp-Fe_{0.91}Ni_{0.09} and Fe_{0.8}Ni_{0.1}Si_{0.1}. Using the equations of state constrained for the same compositions (Morrison et al., 2018), the compressional and shear sound velocities, as well as the shear modulus, of bcc- and hcp-Fe_{0.91}Ni_{0.09} and Fe_{0.8}Ni_{0.1}Si_{0.1} were calculated at 300 K. We find that 9 at% nickel decreases the shear

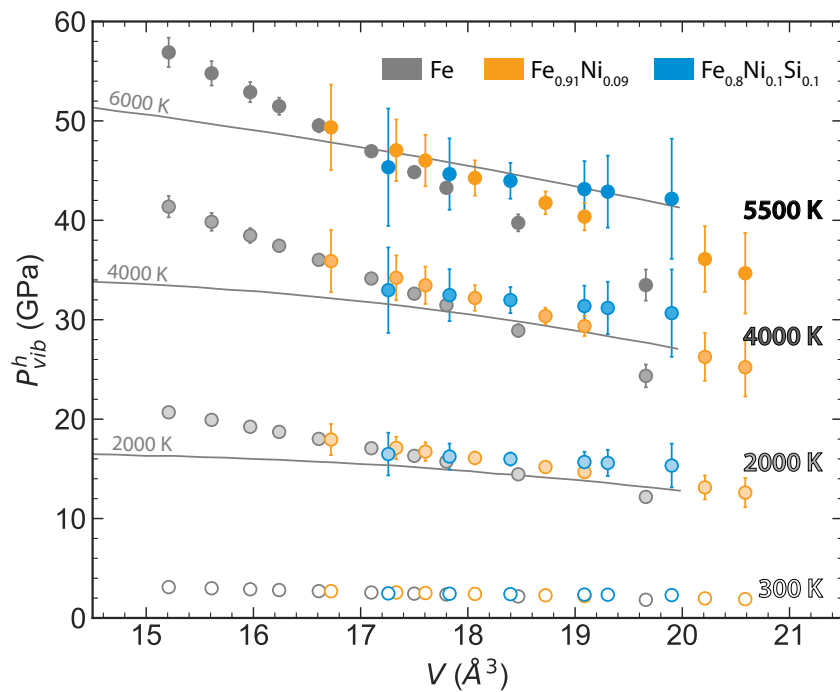


Fig. 19. Harmonic vibrational thermal pressure P_{vib}^h as a function of volume and temperature for hcp-Fe_{0.91}Ni_{0.09}, Fe_{0.8}Ni_{0.1}Si_{0.1}, and Fe at 2000, 4000, and 5500 K (circles). The hcp-Fe data is a re-analysis of data from Murphy et al. (2011b). We compare to ab initio calculations of the harmonic thermal pressure for hcp-Fe by Alfe et al. (2001) at 2000, 4000, and 6000 K (solid lines).

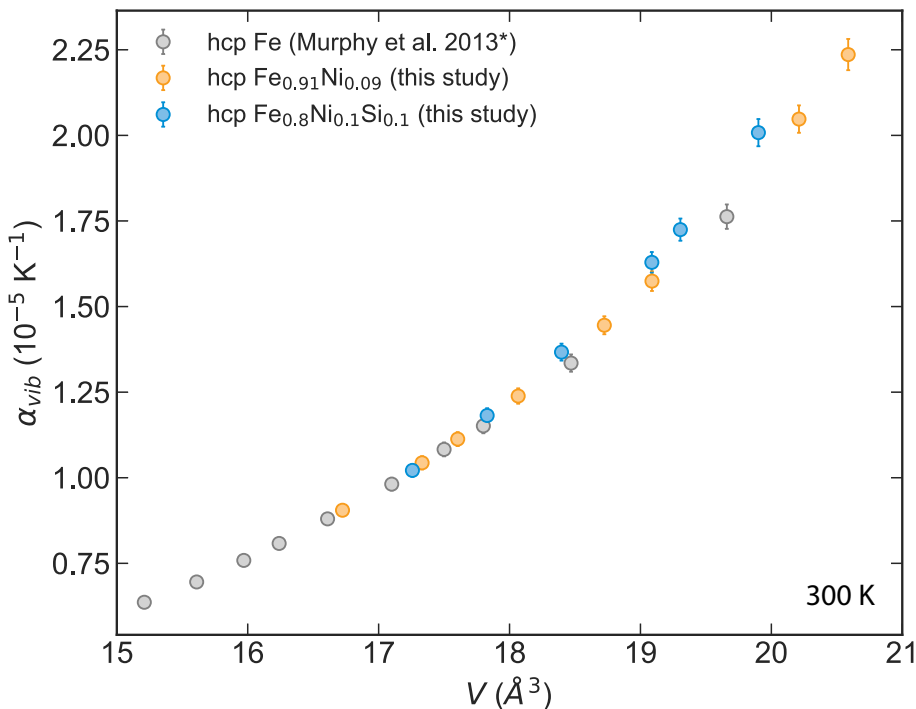


Fig. 20. Vibrational harmonic component of thermal expansion for hcp-Fe_{0.91}Ni_{0.09}, Fe_{0.8}Ni_{0.1}Si_{0.1}, and Fe at 300 K. The data for hcp-Fe is a re-analysis of data from Murphy et al. (2013). If not shown, error bars are smaller than the displayed symbol.

velocity of hcp-iron by $\sim 6\%$, and that silicon has a minimal effect on the shear velocity of hcp-Fe_{0.91}Ni_{0.09}.

From the volume scaling of the phonon DOS, we constrain the 300 K vibrational component of the Grüneisen parameter for hcp-Fe_{0.91}Ni_{0.09} and Fe_{0.8}Ni_{0.1}Si_{0.1}. Within the compression range of the measurements, we find that the Grüneisen parameters of hcp-Fe_{0.91}Ni_{0.09} are similar to those of hcp-Fe, whereas those of Fe_{0.8}Ni_{0.1}Si_{0.1} trend lower. Extrapolation using a Mie-Grüneisen-Debye model with these newly determined values to inner core conditions leads to insignificant deviations from the assumption that these particular alloys have the same Grüneisen parameter and scaling value as hcp-Fe (Morrison et al., 2018). More importantly, we find that the volume dependence of the vibrational free energy of hcp-Fe, which is directly related to the vibrational component of thermal pressure, shows a significant positive deviation from theoretical calculations for hcp-Fe at pressures and temperatures of Earth's core (Fig. 19). The total thermal pressure for iron-alloys under core conditions, most importantly at thousands of Kelvin, must consider the electronic component and, to lesser extent, the anharmonic component (Morrison et al., 2018). These terms, in particular for hcp-iron alloys, are thus far only available from theoretical studies and thus far only reported for hcp-Fe. By combining our experimentally constrained vibrational component with theoretical estimates of the anharmonic and electronic contributions by Alfe et al. (2001), we provide an estimate for the total thermal pressure of hcp-Fe, Fe_{0.91}Ni_{0.09}, and Fe_{0.8}Ni_{0.1}Si_{0.1} at core pressures and temperatures (Table 4).

The phonon DOS also provides access to the vibrational component of entropy per ⁵⁷Fe atom, the volume derivative of which is directly related to the product of isothermal bulk modulus and thermal expansion. Therefore, we can apply the isothermal bulk modulus constrained by Morrison et al. (2018) to determine the vibrational component of thermal expansion for hcp-Fe_{0.91}Ni_{0.09} and Fe_{0.8}Ni_{0.1}Si_{0.1}. The vibrational thermal expansion of hcp-Fe_{0.91}Ni_{0.09} is indistinguishable from that of hcp-iron. Silicon slightly increases the vibrational thermal expansion of Fe_{0.91}Ni_{0.09} at low compressions, but at compressions above 65 GPa, the effect becomes negligible.

Other vibrational properties have been derived from the phonon

DOS, including constraints on the mean-square displacement of the iron atoms. We find that adding 9 at% nickel decreases the Lamb-Mössbauer factor of hcp-iron by $\sim 1\%$, and that silicon has a minimal impact on the Lamb-Mössbauer factor of hcp-Fe_{0.91}Ni_{0.09}. With increasing pressure, the vibrational kinetic energy per ⁵⁷Fe atom of hcp-Fe_{0.91}Ni_{0.09} trends lower than that of hcp-Fe, whereas Fe_{0.8}Ni_{0.1}Si_{0.1} is indistinguishable from that of hcp-Fe. Furthermore, we constrain the vibrational component of specific heat from the phonon DOS. The vibrational specific heat of hcp-Fe_{0.91}Ni_{0.09} trends slightly higher than that of hcp-Fe, while that of Fe_{0.8}Ni_{0.1}Si_{0.1} is indistinguishable from that of hcp-iron. In summary, we present a systematic approach to provide improved constraints on the effects of nickel and silicon on a range of thermo-elastic and vibrational properties of iron, including the sound velocities, all of which are important in modeling the core of Earth and other iron-rich cores of planets.

Acknowledgments

We thank Lisa Mauger and Caitlin Murphy for help with sample synthesis, Dongzhou Zhang and Caitlin Murphy for help during the NRIXS and XRD experiments, and Muir Morrison for helpful discussion of the sound velocity analysis. We thank NSF-EAR-1727020, W.M. Keck Institute for Space Studies, and NDSEG for support of this work. Sector 3 operations, GSECARS sector 13-BM-C, and the gas loading facility are partially supported by COMPRES. Use of APS is supported by the U.S. DOE, Office of Science (DE-AC02-06CH11357). Microprobe analyses were carried out at the Caltech GPS Division Analytical Facility (funded in part by the MRSEC Program of the NSF under DMR-0080065). The data used are listed in the tables, supporting information, and references. The authors have no competing interests to declare.

Appendix A. Supplementary data

Supplementary data to this article can be found online at <https://doi.org/10.1016/j.pepi.2019.05.011>.

References

- Alfè, D., Price, G.D., Gillan, M.J., 2001. Thermodynamics of hexagonal-close-packed iron under Earth's core conditions. *Phys. Rev. B* 64 (045), 123. <https://doi.org/10.1103/PhysRevB.64.045123>.
- Alfè, D., Gillan, M.J., Price, G.D., 2002. Composition and temperature of the earth's core constrained by combining ab initio calculations and seismic data. *Earth Planet. Sci. Lett.* 195 (1–2), 91–98. [https://doi.org/10.1016/S0012-821X\(01\)00568-4](https://doi.org/10.1016/S0012-821X(01)00568-4).
- Alfè, D., Gillan, M.J., Price, G.D., 2007. Temperature and composition of the Earth's core. *Contemp. Phys.* 48 (2), 63–80. <https://doi.org/10.1080/00107510701529653>.
- Allègre, C.J., Poirier, J.P., Humler, E., Hofmann, A.W., 1995. The chemical composition of the Earth. *Earth Planet. Sci. Lett.* 134 (3–4), 515–526. [https://doi.org/10.1016/0012-821X\(95\)00123-T](https://doi.org/10.1016/0012-821X(95)00123-T).
- Allègre, C., Manhes, G., Lewin, E., 2001. Chemical composition of the Earth and the volatility control on planetary genetics. *Earth Planet. Sci. Lett.* 185, 49–69. [https://doi.org/10.1016/S0012-821X\(00\)00359-9](https://doi.org/10.1016/S0012-821X(00)00359-9).
- Antonangeli, D., Occelli, F., Requardt, H., Badro, J., Fiquet, G., Krisch, M., 2004. Elastic anisotropy in textured hcp-iron to 112 GPa from sound wave propagation measurements. *Earth Planet. Sci. Lett.* 225 (1–2), 243–251. <https://doi.org/10.1016/j.epsl.2004.06.004>.
- Antonangeli, D., Siebert, J., Badro, J., Farber, D.L., Fiquet, G., Morard, G., Ryerson, F.J., 2010. Composition of the Earth's inner core from high-pressure sound velocity measurements in Fe–Si alloys. *Earth Planet. Sci. Lett.* 295 (1–2), 292–296. <https://doi.org/10.1016/j.epsl.2010.04.018>.
- Antonangeli, D., Morard, G., Paolasini, L., Garbarino, G., Murphy, C.A., Edmund, E., Decremps, F., Fiquet, G., Bosak, A., Mezouar, M., Fei, Y., 2018. Sound velocities and density measurements of solid hcp-Fe and hcp-Fe–Si (9 wt.%) alloy at high pressure: constraints on the Si abundance in the Earth's inner core. *Earth Planet. Sci. Lett.* 482, 446–453. <https://doi.org/10.1016/j.epsl.2017.11.043>.
- Asanuma, H., Ohtani, E., Sakai, T., Terasaki, H., Kamada, S., Hirao, N., Ohishi, Y., 2011. Static compression of $\text{Fe}_{0.83}\text{Ni}_{0.09}\text{Si}_{0.08}$ alloy to 374 GPa and $\text{Fe}_{0.93}\text{Si}_{0.07}$ alloy to 252 GPa: implications for the Earth's inner core. *Earth Planet. Sci. Lett.* 310 (1–2), 113–118. <https://doi.org/10.1016/j.epsl.2011.06.034>.
- Badro, J., Fiquet, G., Guyot, F., Gregoryanz, E., Occelli, F., Antonangeli, D., D'Astuto, M., 2007. Effect of light elements on the sound velocities in solid iron: implications for the composition of Earth's core. *Earth Planet. Sci. Lett.* 254 (1–2), 233–238. <https://doi.org/10.1016/j.epsl.2006.11.025>.
- Boehler, R., Santamaría-Pérez, D., Errandonea, D., Mezouar, M., 2008. Melting, density, and anisotropy of iron at core conditions: new x-ray measurements to 150 GPa. *J. Phys. Conf. Ser.* 121 (2), 022,018. <https://doi.org/10.1088/1742-6596/121/2/022018>.
- Bouchet, J., Mazevert, S., Morard, G., Guyot, F., Musella, R., 2013. Ab initio equation of state of iron up to 1500 GPa. *Phys. Rev. B* 87, 094,102. <https://doi.org/10.1103/PhysRevB.87.094102>.
- Brown, J.M., McQueen, G., 1986. Phase transitions, Grüneisen parameter, and elasticity for shocked iron between 77 GPa and 400 GPa. *J. Geophys. Res.* 91 (B7), 7485–7494. <https://doi.org/10.1029/JB091iB07p07485>.
- Chen, B., Li, Z., Zhang, D., Liu, J., Hu, M.Y., Zhao, J., Bi, W., Alp, E.E., 2014. Hidden carbon in Earth's inner core revealed by shear softening in dense Fe_2C . *Proc. Natl. Acad. Sci. U. S. A.* 111 (50), 17,755–17,758. <https://doi.org/10.1073/pnas.1411154111>.
- Chen, B., Lai, X., Li, J., Liu, J., Zhao, J., Bi, W., Alp, E.E., Hu, M.Y., Xiao, Y., 2018. Experimental constraints on the sound velocities of cementite Fe_3C to core pressures. *Earth Planet. Sci. Lett.* 494, 164–171. <https://doi.org/10.1016/j.epsl.2018.05.002>.
- Côté, A.S., Vočadlo, L., Dobson, D.P., Alfè, D., Brodholt, J.P., 2010. Ab initio lattice dynamics calculations on the combined effect of temperature and silicon on the stability of different iron phases in the Earth's inner core. *Phys. Earth Planet. Inter.* 178 (1–2), 2–7. <https://doi.org/10.1016/j.pepi.2009.07.004>.
- Côté, A.S., Vočadlo, L., Brodholt, J.P., 2012. Ab initio simulations of iron–nickel alloys at Earth's core conditions. *Earth and Planetary Science Letters* 348, 126–130. <https://doi.org/10.1016/j.epsl.2012.06.025>.
- Decremps, F., Antonangeli, D., Gauthier, M., Ayrinhac, S., Morand, M., LeMarchand, G., Bergame, F., Philippe, J., 2014. Sound velocity of iron up to 152 GPa by picosecond acoustics in diamond anvil cell. *Geophys. Res. Lett.* 41, 1459–1464. <https://doi.org/10.1002/2013GL058859>.
- Deuss, A., 2008. Normal mode constraints on shear and compressional wave velocity of the Earth's inner core. *Earth Planet. Sci. Lett.* 268 (3–4), 364–375. <https://doi.org/10.1016/j.epsl.2008.01.029>.
- Dewaele, A., Loubeyre, P., Occelli, F., Mezouar, M., Dorogokupets, P., Torrent, M., 2006. Quasihydrostatic equation of state of iron above 2 Mbar. *Phys. Rev. Lett.* 97, 215,504. <https://doi.org/10.1103/PhysRevLett.97.215504>.
- Dorogokupets, P.I., Oganov, A.R., 2006. Equations of state of Al, Au, Cu, Pt, Ta, and W and revised ruby pressure scale. *Dokl. Earth Sci.* 410 (1), 1091–1095. <https://doi.org/10.1134/S1028334X06070208>.
- Dubrovinsky, L.S., Saxena, S.K., Lazor, P., 1998. High pressure and high temperature in situ X-ray diffraction study of iron and corundum to 68 GPa using an internally heated diamond anvil cell. *Phys. Chem. Miner.* 25, 434–441. <https://doi.org/10.1007/s002690050133>.
- Dubrovinsky, L.S., S. K. Saxena, N. A. Dubrovinskaia, S. Rekhi, and T. Le Bihan (2000), Grüneisen parameter of ϵ -iron up to 300 GPa from in-situ X-ray study, *Am. Mineral.*, 85(2), 386–389, <https://doi.org/10.2138/am-2000-2-318>.
- Dziewonski, A.M., Anderson, D.L., 1981. Preliminary reference Earth model. *Phys. Earth Planet. Inter.* 25 (4), 297–356. [https://doi.org/10.1016/0031-9201\(81\)90046-7](https://doi.org/10.1016/0031-9201(81)90046-7).
- Ekhholm, M., Mikhaylushkin, A.S., Simak, S.I., Johansson, B., Abrikosov, I.A., 2011. Configurational thermodynamics of Fe–Ni alloys at Earth's core conditions. *Earth Planet. Sci. Lett.* 308 (1–2), 90–96. <https://doi.org/10.1016/j.epsl.2011.05.035>.
- Fei, Y., Murphy, C., Shibasaki, Y., Shahar, A., Huang, H., 2016. Thermal equation of state of hcp-iron: constraint on the density deficit of Earth's solid inner core. *Geophys. Res. Lett.* 43, 6837–6843. <https://doi.org/10.1002/2016GL069456>.
- Fiquet, G., Badro, J., Gregoryanz, E., Fei, Y., Occelli, F., 2009. Sound velocity in iron carbide (Fe_3C) at high pressure: implications for the carbon content of the Earth's inner core. *Phys. Earth Planet. Inter.* 172 (1–2), 125–129. <https://doi.org/10.1016/j.pepi.2008.05.016>.
- Fischer, R.A., Campbell, A.J., 2015. The axial ratio of hcp Fe and Fe–Ni–Si alloys to the conditions of Earth's inner core. *Am. Mineral.* 100 (11–12), 2718–2724. <https://doi.org/10.2138/am-2015-5191>.
- Fischer, R.A., Campbell, A.J., Caracas, R., Reaman, D.M., Dera, P., Prakapenka, V.B., 2012. Equation of state and phase diagram of Fe–16Si alloy as a candidate component of Earth's core. *Earth Planet. Sci. Lett.* 357–358, 268–276. <https://doi.org/10.1016/j.epsl.2012.09.022>.
- Fischer, R.A., Campbell, A.J., Caracas, R., Reaman, D.M., Heinz, D.L., Dera, P., Prakapenka, V.B., 2014. Equations of state in the Fe–FeSi system at high pressures and temperatures. *Journal of Geophysical Research: Solid Earth* 2810–2827. <https://doi.org/10.1002/2013JB010898>.
- Gao, L., Chen, B., Wang, J., Alp, E.E., Zhao, J., Lerche, M., Sturhahn, W., Scott, H.P., Huang, F., Ding, Y., Sinogeikin, S.V., Lundstrom, C.C., Bass, J.D., Li, J., 2008. Pressure-induced magnetic transition and sound velocities of Fe_3C : implications for carbon in the Earth's inner core. *Geophys. Res. Lett.* 35 (17), 1–5. <https://doi.org/10.1029/2008GL034817>.
- Gao, L., Chen, B., Lerche, M., Alp, E.E., Sturhahn, W., Zhao, J., Yavas, H., Li, J., 2009. Sound velocities of compressed Fe_3C from simultaneous synchrotron X-ray diffraction and nuclear resonant scattering measurements. *J. Synchrotron Radiat.* 16 (6), 714–722. <https://doi.org/10.1107/S0909049509033731>.
- Garai, J., Chen, J., Telekes, G., 2011. PVT equation of state of epsilon iron and its densities at inner core conditions. *Am. Mineral.* 96, 828–832. <https://doi.org/10.2138/am.2011.3612>.
- Giefers, H., Lübbers, R., Rupprecht, K., Wortmann, G., Alfè, D., Chumakov, A., 2002. Phonon spectroscopy of oriented hcp iron. *High Pressure Res.* 22, 501–506. <https://doi.org/10.1080/08957950290011437>.
- Gleason, A.E., Mao, W.L., Zhao, J.Y., 2013. Sound velocities for hcp-iron compressed hydrostatically to 136 GPa from phonon density of states. *Geophys. Res. Lett.* 40, 2983–2987. <https://doi.org/10.1002/grl.50588>.
- Hirao, N., Ohtani, E., Kondo, T., Kikegawa, T., 2004. Equation of state of iron–silicon alloys to megabar pressure. *Phys. Chem. Miner.* 31 (6), 329–336. <https://doi.org/10.1007/s00269-004-0387-x>.
- Hirose, K., Labrosse, S., Hernlund, J., 2013. Composition and state of the core. *Annu. Rev. Earth Planet. Sci.* 41 (1), 657–691. <https://doi.org/10.1146/annurev-earth-050212-124007>.
- Hurvich, C.M., Tsai, C.-L., 1989. Regression and time series model selection in small samples. *Biometrika* 76 (2), 297–307. <https://doi.org/10.1093/biomet/76.2.297>.
- Jeanloz, R., 1979. Properties of iron at high pressures and the state of the core. *J. Geophys. Res.* 84 (B11), 6059–6069. <https://doi.org/10.1029/JB084iB11p06059>.
- Kennett, B.L.N., Engdahl, E.R., Buland, R., 1995. Constraints on seismic velocities in the Earth from traveltimes. *Geophys. J. Int.* 122, 108–124. <https://doi.org/10.1111/j.1365-246X.1995.tb03540.x>.
- Lajo, A., Bernard, S., Chiariotti, G.L., Scandolo, S., 2000. Physics of iron at Earth's core conditions. *Science* 287, 1027–1031. <https://doi.org/10.1126/science.287.5455.1027>.
- Li, J., and Y. Fei (2014), Experimental constraints on core composition, in *Treatise on Geochemistry*, vol. 3, edited by H. D. Holland and K. K. Turekian, 2 ed., chap. 15, pp. 527–557, Elsevier Ltd., Amsterdam, Netherlands, <https://doi.org/10.1016/B978-0-08-095975-7.00214-X>.
- Li, Y., Vočadlo, L., Brodholt, J., Wood, I.G., 2016. Thermoelasticity of Fe_7C_3 under inner core conditions. *Journal of Geophysical Research: Solid Earth* 121 (8), 5828–5837. <https://doi.org/10.1002/2016JB013155>.
- Lin, J.-F., 2003. Static compression of iron–silicon alloys: implications for silicon in the Earth's core. *J. Geophys. Res.* 108 (B1), 2045. <https://doi.org/10.1029/2002JB001978>.
- Lin, J.-F., Struzhkin, V.V., Sturhahn, W., Huang, E., Zhao, J., Hu, M.Y., Alp, E.E., Mao, H.-K., Boctor, N., Hemley, R.J., 2003. Sound velocities of iron–nickel and iron–silicon alloys at high pressures. *Geophys. Res. Lett.* 30 (21), 2112. <https://doi.org/10.1029/2003GL018405>.
- Lin, J.-F., Fei, Y., Sturhahn, W., Zhao, J., Mao, H.-K., Hemley, R.J., 2004. Magnetic transition and sound velocities of Fe_3S at high pressure: implications for earth and planetary cores. *Earth Planet. Sci. Lett.* 226, 33–40. <https://doi.org/10.1016/j.epsl.2004.07.018>.
- Lin, J.-F., Sturhahn, W., Zhao, J., Shen, G., Mao, H.-K., Hemley, R.J., 2005. Sound velocities of hot dense iron: Birch's law revisited. *Science* 308, 1892–1894. <https://doi.org/10.1126/science.1111724>.
- Litasov, K.D., Shatskiy, A.F., 2016. Composition of the Earth's core: a review. *Russ. Geol. Geophys.* 57, 22–46. <https://doi.org/10.1016/j.rgg.2016.01.003>.
- Liu, J., Lin, J.-F., Alatas, A., Bi, W., 2014. Sound velocities of bcc-Fe and $\text{Fe}_{0.85}\text{Si}_{0.15}$ alloy at high pressure and temperature. *Phys. Earth Planet. Inter.* 233, 24–32. <https://doi.org/10.1016/j.pepi.2014.05.008>.
- Liu, J., Lin, J.-F., Alatas, A., Bi, W., 2014. Sound velocities of hcp-Fe alloyed with Ni and Si in the Earth's core. *Journal of Geophysical Research: Solid Earth* 121. <https://doi.org/10.1002/2015JB012625>.
- Lübbers, R., Grünsteudel, H.F., Chumakov, A.I., Wortmann, G., 2000. Density of phonon states in iron at high pressure. *Science* 287, 1250–1254. <https://doi.org/10.1126/science.287.5456.1250>.
- Mao, H.K., Wu, Y., Chen, L.C., Shu, J.F., Jephcoat, A.P., 1990. Static compression of iron

- to 300 GPa and Fe0.8Ni0.2 alloy to 260 GPa: Implications for composition of the core. *Journal of Geophysical Research* 95 (B13), 21,737–21,742. <https://doi.org/10.1029/JB095iB13p21737>.
- Mao, H.K., Xu, J., Struzhkin, V.V., Shu, J., Hemley, R.J., Sturhahn, W., Hu, M.Y., Alp, E.E., Vocadlo, L., Alfè, D., Price, G.D., Gillan, M.J., Schwoerer-Böhnig, M., Häusermann, D., Eng, P., Shen, G., Giefers, H., Lübbbers, R., Wortmann, G., 2001. Phonon density of states of iron up to 153 gigapascals. *Science* 292 (914), 914–916. <https://doi.org/10.1126/science.1057670>.
- Mao, W.L., Sturhahn, W., Heinz, D.L., Mao, H.-K., Shu, J., Hemley, R.J., 2004. Nuclear resonant x-ray scattering of iron hydride at high pressure. *Geophys. Res. Lett.* 31, L15,618. <https://doi.org/10.1029/2004GL020541>.
- Mao, W.L., Struzhkin, V.V., Baron, A.Q.R., Tsutsui, S., Tommaseo, C.E., Wenk, H.-R., Hu, M.Y., Chow, P., Sturhahn, W., Shu, J., Hemley, R.J., Heinz, D.L., Mao, H.-K., 2008. Experimental determination of the elasticity of iron at high pressure. *J. Geophys. Res.* 113, B09,213. <https://doi.org/10.1029/2007JB005229>.
- Mao, Z., Lin, J.-F., Liu, J., Alatas, A., Gao, L., Zhao, J., Mao, H.-K., 2012. Sound velocities of Fe and Fe-Si alloy in the Earth's core. *Proc. Natl. Acad. Sci. U. S. A.* 109 (26), 10,239–10,244. <https://doi.org/10.1073/pnas.12070861109>.
- Martorell, B., Brodholt, J., Wood, I.G., Vočadlo, L., 2013a. The effect of nickel on the properties of iron at the conditions of Earth's inner core: ab initio calculations of seismic wave velocities of Fe-Ni alloys. *Earth Planet. Sci. Lett.* 365, 143–151. <https://doi.org/10.1016/j.epsl.2013.01.007>.
- Martorell, B., Vočadlo, L., Brodholt, J., Wood, I.G., 2013b. Strong premelting effect in the elastic properties of hcp-Fe under inner-core conditions. *Science* 342, 466–468. <https://doi.org/10.1126/science.1243651>.
- Martorell, B., Wood, I.G., Brodholt, J., Vočadlo, L., 2016. The elastic properties of hcp-Fe1-xSix at Earth's inner-core conditions. *Earth Planet. Sci. Lett.* 451, 89–96. <https://doi.org/10.1016/j.epsl.2016.07.018>.
- Masters, G., Gubbins, D., 2003. On the resolution of density within the Earth. *Phys. Earth Planet. Inter.* 140 (1–3), 159–167. <https://doi.org/10.1016/j.pepi.2003.07.008>.
- McDonough, W.F., 2003. Compositional model for the Earth's core. In: Carlson, R.W. (Ed.), *Treatise on Geochemistry*. Vol. 2. Elsevier Ltd, Oxford, UK, pp. 547–568. <https://doi.org/10.1016/B0-08-043751-6/02015-6>. (chap. 2.15).
- McDonough, W., Sun, S.S., 1995. The composition of the Earth. *Chem. Geol.* 120, 223–253. [https://doi.org/10.1016/0009-2541\(94\)00140-4](https://doi.org/10.1016/0009-2541(94)00140-4).
- McQueen, R.G., Marsh, S.P., 1966. Shock-wave compression of iron-nickel alloys. *J. Geophys. Res.* 71 (6), 1751–1756. <https://doi.org/10.1029/JZ071i006p01751>.
- Merkel, S., A. F. Goncharov, H.-K. Mao, P. Gillet, and R. J. Hemley (2000), Raman spectroscopy of iron to 152 Gigapascals: implications for Earth's inner core, *Science*, 288, 1626–1629, <https://doi.org/10.1126/science.288.5471.1626>.
- Mori, Y., Ozawa, H., Hirose, K., Sinmyo, R., Tateno, S., Morard, G., Ohishi, Y., 2017. Melting experiments on Fe-Fe₃S system to 254 GPa. *Earth Planet. Sci. Lett.* 464, 135–141. <https://doi.org/10.1016/j.epsl.2017.02.021>.
- Morrison, R.A., Jackson, J.M., Sturhahn, W., Zhang, D., Greenberg, E., 2018. Equations of state and anisotropy of Fe-Ni-Si alloys. *Journal of Geophysical Research: Solid Earth* 123. <https://doi.org/10.1029/2017JB015343>.
- Muñoz, J.A., 2013. *Electronic structure and phonon thermodynamics of iron alloys*, PhD thesis. In: California Institute of Technology.
- Murphy, C.A., Jackson, J.M., Sturhahn, W., Chen, B., 2011a. Grüneisen parameter of hcp-Fe to 171 GPa. *Geophys. Res. Lett.* 38 (24), 1–5. <https://doi.org/10.1029/2011GL049531>.
- Murphy, C.A., Jackson, J.M., Sturhahn, W., Chen, B., 2011b. Melting and thermal pressure of hcp-Fe from the phonon density of states. *Phys. Earth Planet. Inter.* 188, 114–120. <https://doi.org/10.1016/j.pepi.2011.07.001>.
- Murphy, C.A., Jackson, J.M., Sturhahn, W., 2013. Experimental constraints on the thermodynamics and sound velocities of hcp-Fe to core pressures. *Journal of Geophysical Research: Solid Earth* 118. <https://doi.org/10.1002/jgrb.50166>.
- Nguyen, J.H., Holmes, N.C., 2004. Melting of iron at the physical conditions of the Earth's core. *Nature* 427, 339–342. <https://doi.org/10.1038/nature02248>.
- Niu, Z.-W., Zeng, Z.-Y., Cai, L.-C., Chen, X.-R., 2015. Study of the thermodynamic stability of iron at inner core from first-principles theory combined with lattice dynamics. *Phys. Earth Planet. Inter.* 248, 12–19. <https://doi.org/10.1016/j.pepi.2015.09.002>.
- Ohtani, E., Shibasaki, Y., Sakai, T., Mibe, K., Fukui, H., Kamada, S., Sakamaki, T., Seto, Y., Tsutsui, S., Baron, A.Q.R., 2013. Sound velocity of hexagonal close-packed iron up to core pressures. *Geophys. Res. Lett.* 40 (19), 5089–5094. <https://doi.org/10.1002/grl.50992>.
- Ono, S., 2013. Equation of state and elasticity of B2-type FeSi: implications for silicon in the inner core. *Phys. Earth Planet. Inter.* 224, 32–37. <https://doi.org/10.1016/j.pepi.2013.08.009>.
- Ono, S., Kikegawa, T., Ohishi, Y., 2007. Equation of state of the high-pressure polymorph of FeSi to 67 GPa. *Eur. J. Mineral.* 19, 183–187. <https://doi.org/10.1127/0935-1221/2007/0019-1713>.
- Ono, S., Kikegawa, T., Hirao, N., Mibe, K., 2010. High-pressure magnetic transition in hcp-Fe. *Am. Mineral.* 95 (5–6), 880–883. <https://doi.org/10.2138/am.2010.3430>.
- Prescher, C., Prakapenka, V.B., 2015. DIOPTAS: a program for reduction of two-dimensional x-ray diffraction data and data exploration. *High Pressure Res.* 35 (3), 223–230. <https://doi.org/10.1080/08957959.2015.1059835>.
- Ricolleau, A., Fei, Y., Corgne, A., Siebert, J., Badro, J., 2011. Oxygen and silicon contents of Earth's core from high pressure metal-silicate partitioning experiments. *Earth Planet. Sci. Lett.* 310 (3–4), 409–421. <https://doi.org/10.1016/j.epsl.2011.08.004>.
- Sakai, T., Takahashi, S., Nishitani, N., Mashino, I., Ohtani, E., Hirao, N., 2014. Equation of state of pure iron and Fe_{0.9}Ni_{0.1} alloy up to 3 Mbar. *Phys. Earth Planet. Inter.* 228, 114–126. <https://doi.org/10.1016/j.pepi.2013.12.010>.
- Sakai, T., Sakamaki, T., Ohtani, E., Fukui, H., Kamada, S., Tsutsui, S., Uchiyama, H., Baron, A.Q.R., 2018. Sound velocity measurements of hcp Fe-Si alloy at high pressure and high temperature by inelastic X-ray scattering. *Am. Mineral.* 103, 85–90. <https://doi.org/10.2138/am-2018-6072>.
- Sakamaki, T., Ohtani, E., Fukui, H., Kamada, S., Takahashi, S., Sakairi, T., Takahata, A., Sakai, T., Tsutsui, S., Ishikawa, D., Shiraishi, R., Seto, Y., Tsuchiya, T., Baron, A.Q.R., 2016. Constraints on Earth's inner core composition inferred from measurements of the sound velocity of hcp-iron in extreme conditions. *Sci. Adv.* 2, e1500,802. <https://doi.org/10.1126/sciadv.1500802>.
- Sata, N., Hirose, K., Shen, G., Nakajima, Y., Ohishi, Y., Hirao, N., 2010. Compression of FeSi, Fe₃C, Fe_{0.95}O, and FeS under the core pressures and implication for light element in the Earth's core. *Journal of Geophysical Research: Solid Earth* 115 (B09204), 1–13. <https://doi.org/10.1029/2009JB006975>.
- Sha, X., Cohen, R.E., 2010. First-principles thermal equation of state and thermoelasticity of hcp Fe at high pressures. *Phys. Rev. B* 81 (094), 105. <https://doi.org/10.1103/PhysRevB.81.094105>.
- Shibasaki, Y., Ohtani, E., Fukui, H., Sakai, T., Kamada, S., Ishikawa, D., Tsutsui, S., Baron, A.Q.R., Nishitani, N., Hirao, N., Takemura, K., 2012. Sound velocity measurements in dhcp-FeH up to 70 GPa with inelastic X-ray scattering: implications for the composition of the Earth's core. *Earth Planet. Sci. Lett.* 313–314, 79–85. <https://doi.org/10.1016/j.epsl.2011.11.002>.
- Steinle-Neumann, G., Stixrude, L., Cohen, R.E., 1999. First-principles elastic constants for the hcp transition metals Fe, Co, and Re at high pressure. *Phys. Rev. B* 60 (2), 791–799. <https://doi.org/10.1103/PhysRevB.60.791>.
- Steinle-Neumann, G., Stixrude, L., Cohen, R.E., Gülsen, O., 2001. Elasticity of iron at the temperature of the Earth's inner core. *Nature* 413, 57–60. <https://doi.org/10.1038/35092536>.
- Stixrude, L., Wasserman, E., Cohen, R.E., 1997. Composition and temperature of Earth's inner core. *J. Geophys. Res.* 102 (B11), 24,729–24,739. <https://doi.org/10.1029/97JB01215>.
- Sturhahn, W., 2000. CONUSS and PHOENIX: evaluation of nuclear resonant scattering data. *Hyperfine Interactions* 125, 149–172. <https://doi.org/10.1023/A:102681503>.
- Sturhahn, W., 2004. Nuclear resonant spectroscopy. *J. Phys. Condens. Matter* 16 (5), S497–S530. <https://doi.org/10.1088/0953-8984/16/5/009>.
- Sturhahn, W., Jackson, J.M., 2007. Geophysical applications of nuclear resonant spectroscopy. In: Ohtani, E. (Ed.), *Advances in High-pressure Mineralogy: Geological Society of America Special Paper*. 421. Geological Society of America, pp. 157–174. [https://doi.org/10.1130/2007.2421\(09\)](https://doi.org/10.1130/2007.2421(09)).
- Sturhahn, W., and V. G. Kohn (1999), Theoretical aspects of incoherent nuclear resonant scattering, *Hyperfine Interactions*, 123/124, 367–399, <https://doi.org/10.1023/A:1017071806>.
- Takahashi, T., Bassett, W.A., Mao, H.-K., 1968. Isothermal compression of the alloys of iron up to 300 kilobars at room temperature: Iron-nickel alloys. *J. Geophys. Res.* 73 (14), 4717–4725. <https://doi.org/10.1029/JB073i014p04717>.
- Tateno, S., Kuwayama, Y., Hirose, K., Ohishi, Y., 2015. The structure of Fe-Si alloy in Earth's inner core. *Earth Planet. Sci. Lett.* 418, 11–19. <https://doi.org/10.1016/j.epsl.2015.02.008>.
- Thompson, E.C., Davis, A.H., Bi, W., Zhao, J., Alp, E.E., Zhang, D., Greenberg, E., Prakapenka, V.B., Campbell, A.J., 2018. High-pressure geophysical properties of fcc phase FeHx. *Geochim. Geophys. Geosyst.* 19, 305–314. <https://doi.org/10.1002/2017GC007168>.
- Toellner, T.S., 2000. Monochromatization of synchrotron radiation for nuclear resonant scattering experiments. *Hyperfine Interactions* 125, 3–28. <https://doi.org/10.1023/A:1012621317>.
- Tsuchiya, T., Fujibuchi, M., 2009. Effects of Si on the elastic property of Fe at Earth's inner core pressures: first principles study. *Phys. Earth Planet. Inter.* 174, 212–219. <https://doi.org/10.1016/j.pepi.2009.01.007>.
- Uchida, T., Y. Wang, M. L. Rivers, S. R. Sutton, and K. Gpa (2001), Stability field and thermal equation of state of ϵ -iron determined by synchrotron X-ray diffraction in a multianvil apparatus, *J. Geophys. Res.*, 106(B10), 21,799–21,810, <https://doi.org/10.1029/2001JB000258>.
- Vočadlo, L., 2007. Ab initio calculations of the elasticity of iron and iron alloys at inner core conditions: evidence for a partially molten inner core? *Earth Planet. Sci. Lett.* 254 (1–2), 227–232. <https://doi.org/10.1016/j.epsl.2006.09.046>.
- Vočadlo, L., 2015. Earth's core: iron and iron alloys. In: Schubert, G. (Ed.), *Treatise on Geophysics*. Elsevier B.V., Oxford, UK, pp. 117–147. <https://doi.org/10.1016/B978-0-444-53802-4.00032-4>. (chap. 2.06).
- Vočadlo, L., Brodholt, J., Alfè, D., Gillan, M.J., Price, G.D., 2000. Ab initio free energy calculations on the polymorphs of iron at core conditions. *Phys. Earth Planet. Inter.* 117, 123–137. [https://doi.org/10.1016/S0031-9201\(99\)00092-8](https://doi.org/10.1016/S0031-9201(99)00092-8).
- Vočadlo, L., Dobson, D.P., Wood, I.G., 2009. Ab initio calculations of the elasticity of hcp-Fe as a function of temperature at inner-core pressure. *Earth Planet. Sci. Lett.* 288 (3–4), 534–538. <https://doi.org/10.1016/j.epsl.2009.10.015>.
- Wakabayashi, N., Scherm, R.H., Smith, G.H., 1982. Lattice dynamics of Ti, Co, Tc, and other hcp transition metals. *Phys. Rev. B* 25 (8). <https://doi.org/10.1103/PhysRevB.25.5122>.
- Wasserman, E., Stixrude, L., Cohen, R.E., 1996. Thermal properties of iron at high pressures and temperatures. *Phys. Rev. B* 53 (13), 8296–8309. <https://doi.org/10.1103/PhysRevB.53.8296>.
- Wicks, J.K., Jackson, J.M., Sturhahn, W., 2010. Very low sound velocities in iron-rich (Mg,Fe)O: implications for the core-mantle boundary region. *Geophys. Res. Lett.* 37 (15), 1–5. <https://doi.org/10.1029/2010GL043689>.
- Wicks, J.K., Jackson, J.M., Sturhahn, W., Zhang, D., 2017. Sound velocity and density of magnesiowüstites: implications for ultralow-velocity zone topography. *Geophys. Res. Lett.* 44, 2148–2158. <https://doi.org/10.1002/2016GL071225>.
- Wood, B.J., Li, J., Shahar, A., 2013. Carbon in the core: its influence on the properties of core and mantle. *Rev. Mineral. Geochem.* 75 (1), 231–250. <https://doi.org/10.1103/PhysRevB.75.231>.
- Yamazaki, D., E. Ito, T. Yoshino, A. Yoneda, X. Guo, B. Zhang, W. Sun, A. Shimojuku, N.

- Tsujino, T., Kunimoto, Y., Higo, and K. I. Funakoshi (2012), P-V-T equation of state for ϵ -iron up to 80 GPa and 1900 K using the Kawai-type high pressure apparatus equipped with sintered diamond anvils, *Geophys. Res. Lett.*, 39(20), 1–6, <https://doi.org/10.1029/2012GL053540>.
- Zhang, J., Guyot, F., 1999. Thermal equation of state of iron and $\text{Fe}_{0.91}\text{Si}_{0.09}$. *Phys. Chem. Miner.* 26 (3), 206–211. <https://doi.org/10.1007/s002690050178>.
- Zhang, Y.G., Yin, Q.Z., 2012. Carbon and other light element contents in the Earth's core based on first-principles molecular dynamics. *Proc. Natl. Acad. Sci. U. S. A.* 109 (48), 19,579–19,583. <https://doi.org/10.1073/pnas.1203826109>.
- Zhang, Y., Sekine, T., He, H., Yu, Y., Liu, F., Zhang, M., 2014. Shock compression of Fe-Ni-Si system to 280 GPa: implications for the composition of the Earth's outer core. *Geophys. Res. Lett.* 41, 4554–4559. <https://doi.org/10.1002/2014GL060670>.
- Zhang, D., Jackson, J.M., Zhao, J., Sturhahn, W., Alp, E.E., Hu, M.Y., Toellner, T.S., Murphy, C.A., Prakapenka, V.B., 2016. Temperature of Earth's core constrained from melting of Fe and $\text{Fe}_{0.9}\text{Ni}_{0.1}$ at high pressures. *Earth Planet. Sci. Lett.* 447, 72–83. <https://doi.org/10.1016/j.epsl.2016.04.026>.